Full-Rank Unsupervised Node Embeddings for Directed Graphs via Message Aggregation

Anonymous authors
Paper under double-blind review

Abstract

Linear message-passing models have emerged as compelling alternatives to non-linear graph neural networks for unsupervised node embedding learning, due to their scalability and competitive performance on downstream tasks. However, we identify a fundamental flaw in recently proposed linear models that combine embedding aggregation with concatenation during each message-passing iteration: rank deficiency. A rank-deficient embedding matrix contains column vectors which take arbitrary values, leading to ill-conditioning that degrades downstream task accuracy, particularly in unsupervised tasks such as graph alignment. We deduce that repeated embedding aggregation and concatenation introduces linearly dependent features, causing rank deficiency. To address this, we propose ACC (Aggregate, Compress, Concatenate), a novel model that avoids redundant feature computation by applying aggregation to the messages from the previous iteration, rather than the embeddings. Consequently, ACC generates full-rank embeddings, significantly improving graph alignment accuracy from 10% to 60% compared to rank-deficient embeddings, while also being faster to compute. Additionally, ACC employs directed message-passing and achieves node classification accuracies comparable to state-of-the-art self-supervised graph neural networks on directed graph benchmarks, while also being over 70 times faster on graphs with over 1 million edges.

1 Introduction

Node embeddings, which represent nodes in a graph as vectors, have proven highly effective for various graph-related tasks, including node classification (Veličković et al., 2018; Rossi et al., 2023), node clustering (Henderson et al., 2012; Donnat et al., 2018), and graph alignment (Heimann et al., 2018; Skitsas et al., 2023). Consequently, there has been substantial research focused on developing algorithms to compute these embeddings, resulting in a wide array of models (Kipf & Welling, 2017; Wu et al., 2019; 2021; Rossi et al., 2023).

Given the scarcity of labelled data in real-world graphs (Veličković et al., 2019), our work focuses on unsupervised embedding models. Unlike supervised models, which are designed for specific downstream tasks, unsupervised models aim to extract and compress the information inherent in the graph structure into individual embedding vectors. The dominant approach for this extraction is *message-passing* (Gilmer et al., 2017).

In a message-passing algorithm, each node is initially assigned a feature vector, serving as its initial embedding. These embeddings are iteratively refined by incorporating information from increasingly larger neighbourhoods. Conceptually, each iteration consists of two steps: the aggregation step, where information from a node's neighbourhood is summarized into a message, and the update step, where these messages are integrated into the existing embeddings.

When the aggregation and update steps consist of parameterized and non-linear functions, the message-passing model is referred to as a Graph Neural Network (GNN) (Wu et al., 2021). While the parameterization and non-linearity of GNNs make them highly expressive, these features also limit their scalability. Training GNNs requires non-convex optimization, typically through gradient descent, to minimize a self-supervised loss function. This training process involves hundreds or even thousands of training epochs, each consisting of multiple message-passing iterations (Zhang et al., 2021; Thakoor et al., 2022; Hou et al., 2022; 2023).

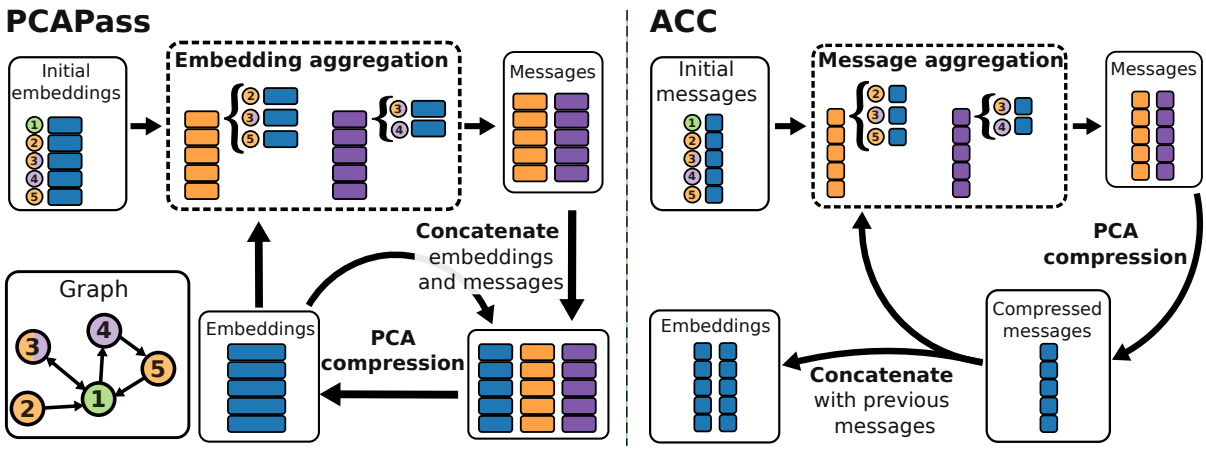

Figure 1: Overview of directed message-passing in PCAPass (Sadowski et al., 2022) and our model, ACC. Each vertically stacked rectangle represents a matrix row corresponding to a node in the graph (bottom-left). The representations are colour-coded: blue for node embeddings, and orange and purple for messages. Orange denotes aggregation following edge directions, while purple indicates reverse-direction aggregation. Node 1, highlighted in green in the graph, is used to illustrate these aggregations. In PCAPass, messages are concatenated with the embeddings from the previous iteration, creating a feedback loop that leads to feature duplication and rank deficiency over multiple iterations. ACC avoids this issue through message aggregation, where only the message matrices are propagated between iterations. The embedding matrix is constructed by concatenating the messages outside the feedback loop.

In their seminal work, Wu et al. (2019) addressed the scalability challenge of GNNs by introducing a linear message-passing model called SGCN. They demonstrated that SGCN could achieve accuracies comparable to GNNs on popular node classification benchmarks while being significantly more scalable, requiring only a single execution of the message-passing procedure. However, despite these advancements, SGCN encounters a common issue in message-passing models: over-smoothing (Li et al., 2018; Chen et al., 2020), where the repeated summation of embeddings across iterations leads to a gradual loss of information.

Computing *multi-scale* embeddings, i.e., concatenating vectors that capture information from various neighbourhood sizes, is a common method for mitigating information loss in unsupervised node embedding models (Tang et al., 2015; Cao et al., 2015; Perozzi et al., 2017; Donnat et al., 2018; Rozemberczki et al., 2021). A recent example of this approach is PCAPass (Sadowski et al., 2022). As shown on the left in Figure 1, PCAPass aggregates node embeddings in each message-passing iteration to create new features, called messages, which are then combined with the existing embeddings via horizontal concatenation. To prevent the embedding dimensionality from doubling with each iteration, the concatenated matrix is compressed using PCA.

While the concatenation approach addresses over-smoothing, it introduces a new issue: rank deficiency (Hansen, 1998, Ch. 1). A rank-deficient matrix is characterized by a cluster of singular values close to zero, each corresponding to an arbitrary and non-informative feature column. This phenomenon affects the PCAPass embedding matrix and degrades the quality of the embeddings. Unsupervised downstream tasks, which rely on distances between embeddings, are particularly sensitive to this issue, raising concerns since such tasks are well-suited for unsupervised node embedding models.

We identify that the repeated embedding aggregation and concatenation in PCAPass leads to the creation of linearly dependent features, which results in rank deficiency. To address this, we propose ACC[1] (Aggregate, Compress, Concatenate), a linear message-passing model designed to prevent rank deficiency while maintaining scalability by generating embeddings in a single forward pass. As shown in Figure 1, ACC applies aggregation and PCA compression to the *message matrices* from the previous iteration, rather than the embeddings, and constructs the embeddings via concatenation separately. This *message aggregation* approach breaks the feedback loop present in PCAPass, and thereby avoids computing the redundant features that cause rank deficiency.

[1]Anonymized code for ACC and our experiments is available [here] and [here]

In support of ACC, we demonstrate the rank deficiency issue present in PCAPass, focusing particularly on its negative impact on unsupervised embedding-based graph alignment (Heimann et al., 2018). Although it is technically possible to address the rank deficiency in PCAPass through singular value thresholding, this approach is not only difficult due to numerical inaccuracies but also inefficient, as computation is used to generate the redundant features in the first place. Consequently, ACC consistently achieves higher graph alignment accuracies and computes embeddings faster than PCAPass.

We also demonstrate ACC's effectiveness in learning node embeddings on directed graphs, an underexplored challenge for unsupervised message-passing models that has only recently been addressed in the supervised learning context (Rossi et al., 2023). Using standard directed graph node classification benchmarks without hyperparameter tuning, we show that ACC achieves accuracies comparable to state-of-the-art self-supervised GNNs. Notably, ACC is significantly faster, at least 70 times faster on the Arxiv Year dataset (Lim et al., 2021) with GPU computations and 270 times faster on Snap Patents (Leskovec et al., 2005) with CPU.

2 Background: Node embeddings via message-passing and embedding aggregation

The message-passing framework (Gilmer et al., 2017) forms the basis for a wide range of graph models (Kipf & Welling, 2017; Hamilton et al., 2017; Wu et al., 2019), including our model, ACC. In this section, we introduce the principles and mathematical notation for node embedding learning through message-passing, followed by a description of the embedding aggregation and concatenation approach used by Sadowski et al. (2022) for PCAPass. Additionally, we outline directed message-passing for PCAPass, following Rossi et al. (2023).

Node embedding message-passing models take as input a graph $\mathcal{G} = (\mathbb{N}, \mathbb{M})$ and a matrix $\boldsymbol{X} \in \mathbb{R}^{n \times d}$, and output an embedding matrix $\boldsymbol{Z} \in \mathbb{R}^{n \times p}$. The graph $\mathcal{G}$ consists of n nodes $\mathbb{N}$, with $n = |\mathbb{N}|$, connected by m edges $\mathbb{M}$, where $m = |\mathbb{M}|$. The matrix $\boldsymbol{X}$ contains initial feature vectors of length d for each node, and the embedding matrix $\boldsymbol{Z}$ holds the resulting p-dimensional node embeddings. In this work, we assume a transductive setting where $\mathcal{G}$ is fully observed during the computation of $\boldsymbol{Z}$, which is common in unsupervised node embedding models (Zhang et al., 2021; Thakoor et al., 2022; Hou et al., 2022; Sadowski et al., 2022).

The goal of message-passing is to gather graph structure information into the embeddings of each node. This is achieved by iteratively updating each node embedding by incorporating information from the nodes' respective neighbourhood, resulting in a sequence of progressively refined embedding matrices. We denote the embedding matrix after k message-passing iterations as $\boldsymbol{H}^{(k)} \in \mathbb{R}^{n \times p_k}$, where the embedding dimensionality p_k may vary across iterations. The final embeddings are obtained after K iterations, represented as $\boldsymbol{Z} = \boldsymbol{H}^{(K)}$.

Each message-passing iteration consists of two key steps: *aggregation* and *update*. In the aggregation step, each node collects information from its immediate neighbours, aggregating these inputs into a new vector called a message. We denote the matrix of all messages at iteration k as $\boldsymbol{M}^{(k)}$. In the update step, each node integrates the new information by combining its received message with its current embeddings. This iterative process allows information to propagate through the graph, enabling each node to gather data from increasingly distant nodes, effectively expanding its receptive field with each iteration.

We now describe the aggregation and update operations used by PCAPass in detail. Let $\boldsymbol{A} \in \mathbb{R}^{n \times n}$ represent the graph's adjacency matrix, where the element $A_{i,j}$ indicates the presence of an edge from node j to node i. The out-degree and in-degree of node i are denoted as $\deg_{\mathtt{O}}(i)$ and $\deg_{\mathtt{I}}(i)$, respectively:

$$A_{i,j} = \begin{cases} 1 & \text{if } (j,i) \in \mathbb{M}, \\ 0 & \text{otherwise,} \end{cases} \qquad \deg_{\mathtt{O}}(i) = \sum_{k=1}^{n} A_{k,i}, \qquad \deg_{\mathtt{I}}(i) = \sum_{k=1}^{n} A_{i,k}. \tag{1}$$

Additionally, let $\boldsymbol{D}_{\mathtt{O}}$ be a diagonal matrix containing the out-degrees, with $D_{\mathtt{O}_{i,i}} = \deg_{\mathtt{O}}(i)$, and similarly, let $\boldsymbol{D}_{\mathtt{I}}$ be a diagonal matrix of in-degrees. The matrices $\boldsymbol{D}_{\mathtt{O}}^{-1}$ and $\boldsymbol{D}_{\mathtt{I}}^{-1}$ represent their respective inverses, with elements corresponding to nodes with zero out-degree or in-degree set to 0.

For undirected graphs, the adjacency matrix is symmetric, $\boldsymbol{A} = \boldsymbol{A}^{\intercal}$, and each node has a single degree, so $\boldsymbol{D} = \boldsymbol{D}_{\mathtt{O}} = \boldsymbol{D}_{\mathtt{I}}$. The normalized adjacency matrix is then defined as $\boldsymbol{A}_{\mathtt{N}} = \boldsymbol{D}^{-1}\boldsymbol{A}$. Using the above definitions, the embedding aggregation step used by PCAPass can be formulated as $\boldsymbol{M}^{(k)} = \boldsymbol{A}_{\mathtt{N}}\boldsymbol{H}^{(k-1)}$, where the message for node i, $\boldsymbol{M}^{(k)}_{i,:}$, is the average of its neighbours' embeddings.

PCAPass updates its embeddings in each iteration using a concatenation and compression approach. This update can be expressed as $\boldsymbol{H}^{(k)} = \begin{bmatrix}\boldsymbol{H}^{(k-1)} & \boldsymbol{M}^{(k)}\end{bmatrix}\boldsymbol{V}^{(k)}$, where the brackets indicate horizontal concatenation. The matrix $\boldsymbol{V}^{(k)} \in \mathbb{R}^{2p_{k-1}\times p_k}$ is derived through PCA (Murphy, 2012, Ch. 12.2) and serves to compress the embeddings. Compression is essential because, without it, the dimensionality of the embedding space would double with each message-passing iteration, resulting in a final dimension of $2^K d$. This exponential growth would impose considerable memory and computational overhead, and could negatively impact downstream tasks due to the curse of dimensionality.

Although Sadowski et al. (2022) originally formulated PCAPass for undirected graphs, it can be straightforwardly extended to directed graphs by following the approach of Rossi et al. (2023). In directed graphs, each node has two distinct sets of neighbours: those connected by incoming edges and those connected by outgoing edges. To capture the information from these distinct neighbourhoods, two separate aggregation operators are employed: $\boldsymbol{A}_{\mathtt{F}} = \boldsymbol{D}_{\mathtt{I}}^{-1}\boldsymbol{A}$ and $\boldsymbol{A}_{\mathtt{B}} = \boldsymbol{D}_{\mathtt{O}}^{-1}\boldsymbol{A}^{\intercal}$. Here, $\boldsymbol{A}_{\mathtt{F}}$ uses the adjacency matrix $\boldsymbol{A}$, while $\boldsymbol{A}_{\mathtt{B}}$ uses its transpose $\boldsymbol{A}^{\intercal}$, corresponding to a graph where all edge directions are reversed. The forward operator $\boldsymbol{A}_{\mathtt{F}}$ aggregates messages based on a node's incoming edges and normalizes by in-degree, while the backward operator $\boldsymbol{A}_{\mathtt{B}}$ aggregates based on outgoing edges and normalizes by out-degree.

With these operators, the directed aggregation step for PCAPass is defined as $\boldsymbol{M}_{\mathtt{F}}^{(k)} = \boldsymbol{A}_{\mathtt{F}}\boldsymbol{H}^{(k-1)}$ and $\boldsymbol{M}_{\mathtt{B}}^{(k)} = \boldsymbol{A}_{\mathtt{B}}\boldsymbol{H}^{(k-1)}$. In the update step, both forward and backward messages are concatenated with the previous embeddings and compressed: $\boldsymbol{H}^{(k)} = \begin{bmatrix}\boldsymbol{H}^{(k-1)} & \boldsymbol{M}_{\mathtt{F}}^{(k)} & \boldsymbol{M}_{\mathtt{B}}^{(k)}\end{bmatrix}\boldsymbol{V}^{(k)}$, with $\boldsymbol{V}^{(k)} \in \mathbb{R}^{3p_{k-1}\times p_k}$.

3 Embedding aggregation and concatenation results in rank deficiency

As outlined above, PCAPass (Sadowski et al., 2022) leverages embedding aggregation, concatenation, and compression to generate node embeddings. This approach aims to address the over-smoothing issue that often plagues message-passing models (Li et al., 2018; Chen et al., 2020). However, the repeated process of embedding aggregation and concatenation introduces and retains redundant features in the embeddings. This not only leads to inefficient computation but also results in *rank deficiency*, a condition where the embedding matrix becomes ill-conditioned, adversely affecting the quality and usefulness of the embeddings.

3.1 Origin of rank deficiency

A matrix $\boldsymbol{Z} \in \mathbb{R}^{n\times p}$ is considered rank-deficient if it exhibits a cluster of small singular values, with a clear gap between the large and small singular values (Hansen, 1998, Ch. 1.). This situation arises when the columns of $\boldsymbol{Z}$ are not linearly independent, indicating the presence of redundant features.

To illustrate the relationship between redundant features and small singular values, consider a simple example. Let $\boldsymbol{X} \in \mathbb{R}^{n\times d}$ be a full-rank matrix with the singular value decomposition (SVD) $\boldsymbol{X} = \boldsymbol{U}\boldsymbol{\Sigma}\boldsymbol{V}^{\intercal}$. Here, $\boldsymbol{U} \in \mathbb{R}^{n\times d}$ and $\boldsymbol{V} \in \mathbb{R}^{d\times d}$ have orthogonal columns with unit norms, and $\boldsymbol{\Sigma}$ is a non-negative diagonal matrix containing the singular values in descending order (Golub & Van Loan, 2013, Ch. 2.4).

Now, define a matrix $\boldsymbol{Z} = \begin{bmatrix}\boldsymbol{X} & \boldsymbol{X}\end{bmatrix} \in \mathbb{R}^{n\times 2d}$, where each column of $\boldsymbol{X}$ is duplicated, making the last d columns in $\boldsymbol{Z}$ redundant. The SVD of $\boldsymbol{Z}$ can then be expressed as $\boldsymbol{Z} = \boldsymbol{U}_{\boldsymbol{Z}}\boldsymbol{\Sigma}_{\boldsymbol{Z}}\boldsymbol{V}_{\boldsymbol{Z}}^{\intercal}$, where

$$\boldsymbol{U}_{\boldsymbol{Z}} = \begin{bmatrix}\boldsymbol{U} & \boldsymbol{\Upsilon}_{\boldsymbol{U}}\end{bmatrix}, \qquad \boldsymbol{\Sigma}_{\boldsymbol{Z}} = \begin{bmatrix}\sqrt{2}\boldsymbol{\Sigma} & \boldsymbol{0} \\ \boldsymbol{0} & \boldsymbol{0}\end{bmatrix}, \qquad \boldsymbol{V}_{\boldsymbol{Z}}^{\intercal} = \frac{1}{\sqrt{2}}\begin{bmatrix}\boldsymbol{V}^{\intercal} & \boldsymbol{V}^{\intercal} \\ \boldsymbol{\Upsilon}_{\boldsymbol{V}_1}^{\intercal} & \boldsymbol{\Upsilon}_{\boldsymbol{V}_2}^{\intercal}\end{bmatrix}. \tag{2}$$

Here, the block matrices $\boldsymbol{\Upsilon}_{\boldsymbol{U}} \in \mathbb{R}^{n\times d}$, $\boldsymbol{\Upsilon}_{\boldsymbol{V}_1} \in \mathbb{R}^{d\times d}$, and $\boldsymbol{\Upsilon}_{\boldsymbol{V}_2} \in \mathbb{R}^{d\times d}$ are orthonormal and satisfy $\boldsymbol{\Upsilon}_{\boldsymbol{U}}^{\intercal}\boldsymbol{U} = \boldsymbol{0}$ and $\boldsymbol{\Upsilon}_{\boldsymbol{V}_1}^{\intercal}\boldsymbol{V} = \boldsymbol{\Upsilon}_{\boldsymbol{V}_2}^{\intercal}\boldsymbol{V} = \boldsymbol{0}$. We can verify this decomposition through matrix multiplication:

$$\boldsymbol{U}_{\boldsymbol{Z}}\boldsymbol{\Sigma}_{\boldsymbol{Z}}\boldsymbol{V}_{\boldsymbol{Z}}^{\intercal} = \begin{bmatrix}\boldsymbol{U} & \boldsymbol{\Upsilon}_{\boldsymbol{U}}\end{bmatrix}\begin{bmatrix}\sqrt{2}\boldsymbol{\Sigma} & \boldsymbol{0} \\ \boldsymbol{0} & \boldsymbol{0}\end{bmatrix}\frac{1}{\sqrt{2}}\begin{bmatrix}\boldsymbol{V}^{\intercal} & \boldsymbol{V}^{\intercal} \\ \boldsymbol{\Upsilon}_{\boldsymbol{V}_1}^{\intercal} & \boldsymbol{\Upsilon}_{\boldsymbol{V}_2}^{\intercal}\end{bmatrix} = \begin{bmatrix}\boldsymbol{U}\boldsymbol{\Sigma} & \boldsymbol{0}\end{bmatrix}\begin{bmatrix}\boldsymbol{V}^{\intercal} & \boldsymbol{V}^{\intercal} \\ \boldsymbol{\Upsilon}_{\boldsymbol{V}_1}^{\intercal} & \boldsymbol{\Upsilon}_{\boldsymbol{V}_2}^{\intercal}\end{bmatrix} = \begin{bmatrix}\boldsymbol{U}\boldsymbol{\Sigma}\boldsymbol{V}^{\intercal} & \boldsymbol{U}\boldsymbol{\Sigma}\boldsymbol{V}^{\intercal}\end{bmatrix}. \tag{3}$$

(See Appendix A for verification of the orthonormality of $\boldsymbol{U}_{\boldsymbol{Z}}$ and $\boldsymbol{V}_{\boldsymbol{Z}}$.)

The expression for $\boldsymbol{\Sigma}_{\boldsymbol{Z}}$ in Equation 2 reveals two clusters of singular values: the d values contained in $\boldsymbol{\Sigma}$ and d singular values equal to zero. Each of the zero singular values corresponds to a column in $\boldsymbol{\Upsilon}_{\boldsymbol{U}}$, which

we refer to as singular dimensions. These singular dimensions span the left null space of $\boldsymbol{Z}$ and do not contain any information about $\boldsymbol{X}$. All information about $\boldsymbol{X}$ is already encapsulated in $\boldsymbol{U}$, $\boldsymbol{\Sigma}$, and $\boldsymbol{V}$, as demonstrated by Equation 3. The columns of $\boldsymbol{\Upsilon}_{\boldsymbol{U}}$ are only constrained by their orthogonality to the columns in $\boldsymbol{U}$, and their elements can otherwise be chosen arbitrarily. Similarly, $\boldsymbol{\Upsilon}_{\boldsymbol{V}_1}$ and $\boldsymbol{\Upsilon}_{\boldsymbol{V}_2}$ are only constrained by their orthogonality to $\boldsymbol{V}$.

Although the values of $\boldsymbol{\Upsilon}_{\boldsymbol{U}}$, $\boldsymbol{\Upsilon}_{\boldsymbol{V}_1}$, and $\boldsymbol{\Upsilon}_{\boldsymbol{V}_2}$ are not uniquely defined, in practical applications, they are determined by a combination of numerical inaccuracies and the arbitrary implementation choices of the specific algorithm used to compute the SVD. Since they do not carry any meaningful information about $\boldsymbol{X}$, they can effectively be considered noise. Furthermore, numerical implementations of SVD will not produce singular values that are exactly zero due to rounding errors, as reflected in the definition of rank deficiency.

3.2 Rank deficiency in PCAPass

Having established the connection between redundant features and rank deficiency, we now analyse the message-passing mechanism in PCAPass, as described in Section 2, to show how redundant features contribute to rank deficiency in its embeddings. For simplicity, we focus on undirected message-passing; however, the results readily extend to directed graphs.

Let p_k denote the dimension of the embeddings after compression in the kth iteration, with $p_0 = d$, and let $\boldsymbol{W}^{(k)} \in \mathbb{R}^{2p_{k-1} \times p_k}$ denote the compression matrix for iteration k. Then, the PCAPass message-passing update step can be expressed as $\boldsymbol{H}^{(k)} = \begin{bmatrix}\boldsymbol{H}^{(k-1)} & \boldsymbol{A}_{\mathtt{N}}\boldsymbol{H}^{(k-1)}\end{bmatrix}\boldsymbol{W}^{(k)}$,with the first two iterations given by

$$\begin{aligned}\boldsymbol{H}^{(1)} &= \begin{bmatrix}\boldsymbol{X} & \boldsymbol{A}_{\mathtt{N}}\boldsymbol{X}\end{bmatrix}\boldsymbol{W}^{(1)},\\ \boldsymbol{H}^{(2)} &= \begin{bmatrix}\boldsymbol{H}^{(1)} & \boldsymbol{A}_{\mathtt{N}}\boldsymbol{H}^{(1)}\end{bmatrix}\boldsymbol{W}^{(2)}.\end{aligned} \tag{4}$$

By inserting $\boldsymbol{H}^{(1)}$ into the expression for $\boldsymbol{H}^{(2)}$, and factoring out $\boldsymbol{W}^{(1)}$, we obtain the following result:

$$\begin{aligned}\boldsymbol{H}^{(2)} &= \begin{bmatrix}\boldsymbol{H}^{(1)} & \boldsymbol{A}_{\mathtt{N}}\boldsymbol{H}^{(1)}\end{bmatrix}\boldsymbol{W}^{(2)}\\ &= \begin{bmatrix}\begin{bmatrix}\boldsymbol{X} & \boldsymbol{A}_{\mathtt{N}}\boldsymbol{X}\end{bmatrix}\boldsymbol{W}^{(1)} & \boldsymbol{A}_{\mathtt{N}}\begin{bmatrix}\boldsymbol{X} & \boldsymbol{A}_{\mathtt{N}}\boldsymbol{X}\end{bmatrix}\boldsymbol{W}^{(1)}\end{bmatrix}\boldsymbol{W}^{(2)}\\ &= \begin{bmatrix}\boldsymbol{X} & \boldsymbol{A}_{\mathtt{N}}\boldsymbol{X} & \boldsymbol{A}_{\mathtt{N}}\boldsymbol{X} & \boldsymbol{A}_{\mathtt{N}}^2\boldsymbol{X}\end{bmatrix}\begin{bmatrix}\boldsymbol{W}^{(1)} & \boldsymbol{0}\\ \boldsymbol{0} & \boldsymbol{W}^{(1)}\end{bmatrix}\boldsymbol{W}^{(2)}\\ &= \boldsymbol{A}_{\boldsymbol{X}}^{(2)}\hat{\boldsymbol{W}}^{(2)},\end{aligned} \tag{5}$$

$$\boldsymbol{A}_{\boldsymbol{X}}^{(2)} = \begin{bmatrix}\boldsymbol{X} & \boldsymbol{A}_{\mathtt{N}}\boldsymbol{X} & \boldsymbol{A}_{\mathtt{N}}\boldsymbol{X} & \boldsymbol{A}_{\mathtt{N}}^2\boldsymbol{X}\end{bmatrix} \in \mathbb{R}^{n\times 4d}, \tag{6}$$

$$\hat{\boldsymbol{W}}^{(2)} = \begin{bmatrix}\boldsymbol{W}^{(1)} & \boldsymbol{0}\\ \boldsymbol{0} & \boldsymbol{W}^{(1)}\end{bmatrix}\boldsymbol{W}^{(2)} \in \mathbb{R}^{4d\times p_2}. \tag{7}$$

We see that $\boldsymbol{H}^{(2)} = \boldsymbol{A}_{\boldsymbol{X}}^{(2)}\hat{\boldsymbol{W}}^{(2)}$, where $\boldsymbol{A}_{\boldsymbol{X}}^{(2)}$ consists of four submatrices of aggregated node features. We can express $\boldsymbol{H}^{(3)}$ on the same block matrix form:

$$\begin{aligned}\boldsymbol{H}^{(3)} &= \begin{bmatrix}\boldsymbol{H}^{(2)} & \boldsymbol{A}_{\mathtt{N}}\boldsymbol{H}^{(2)}\end{bmatrix}\boldsymbol{W}^{(3)}\\ &= \begin{bmatrix}\boldsymbol{X} & \boldsymbol{A}_{\mathtt{N}}\boldsymbol{X} & \boldsymbol{A}_{\mathtt{N}}\boldsymbol{X} & \boldsymbol{A}_{\mathtt{N}}^2\boldsymbol{X} & \boldsymbol{A}_{\mathtt{N}}\boldsymbol{X} & \boldsymbol{A}_{\mathtt{N}}^2\boldsymbol{X} & \boldsymbol{A}_{\mathtt{N}}^2\boldsymbol{X} & \boldsymbol{A}_{\mathtt{N}}^3\boldsymbol{X}\end{bmatrix}\begin{bmatrix}\hat{\boldsymbol{W}}^{(2)} & \boldsymbol{0}\\ \boldsymbol{0} & \hat{\boldsymbol{W}}^{(2)}\end{bmatrix}\boldsymbol{W}^{(3)}\\ &= \boldsymbol{A}_{\boldsymbol{X}}^{(3)}\hat{\boldsymbol{W}}^{(3)},\end{aligned} \tag{8}$$

$$\boldsymbol{A}_{\boldsymbol{X}}^{(3)} = \begin{bmatrix}\boldsymbol{X} & \boldsymbol{A}_{\mathtt{N}}\boldsymbol{X} & \boldsymbol{A}_{\mathtt{N}}\boldsymbol{X} & \boldsymbol{A}_{\mathtt{N}}^2\boldsymbol{X} & \boldsymbol{A}_{\mathtt{N}}\boldsymbol{X} & \boldsymbol{A}_{\mathtt{N}}^2\boldsymbol{X} & \boldsymbol{A}_{\mathtt{N}}^2\boldsymbol{X} & \boldsymbol{A}_{\mathtt{N}}^3\boldsymbol{X}\end{bmatrix} \in \mathbb{R}^{n\times 8d}, \tag{9}$$

$$\hat{\boldsymbol{W}}^{(3)} = \begin{bmatrix}\hat{\boldsymbol{W}}^{(2)} & \boldsymbol{0}\\ \boldsymbol{0} & \hat{\boldsymbol{W}}^{(2)}\end{bmatrix}\boldsymbol{W}^{(3)} \in \mathbb{R}^{8d\times p_3}. \tag{10}$$

Continuing this pattern, we see that $\boldsymbol{H}^{(k)} = \boldsymbol{A}_{\boldsymbol{X}}^{(k)}\hat{\boldsymbol{W}}^{(k)}$, where $\boldsymbol{A}_{\boldsymbol{X}}^{(k)} \in \mathbb{R}^{n\times 2^k d}$ and $\hat{\boldsymbol{W}}^{(k)} \in \mathbb{R}^{2^k d\times p_k}$.

Notice that the submatrix $\boldsymbol{A}_{\mathtt{N}}\boldsymbol{X}$ is repeated twice in $\boldsymbol{A}_{\boldsymbol{X}}^{(2)}$ and three times in $\boldsymbol{A}_{\boldsymbol{X}}^{(3)}$, where $\boldsymbol{A}_{\mathtt{N}}^2\boldsymbol{X}$ also appears three times. These redundant submatrices contribute to the rank deficiency of the PCAPass embeddings.

In fact, only one linearly independent submatrix is introduced in each message-passing iteration, specifically $\boldsymbol{A}_{\mathrm{N}}^{k}\boldsymbol{X}$ in iteration k, implying that $\mathrm{rank}(\boldsymbol{A}_{\boldsymbol{X}}^{(k)}) \leq (k+1)d$. Consequently, we can obtain an upper bound on the rank of $\boldsymbol{H}^{(k)}$ by applying Sylvester's inequality (Horn & Johnson, 2012, Ch. 0.4.5):

$$\mathrm{rank}(\boldsymbol{H}^{(k)}) \leq \min(\mathrm{rank}(\boldsymbol{A}_{\boldsymbol{X}}^{(k)}), \mathrm{rank}(\hat{\boldsymbol{W}}^{(k)})) \leq \mathrm{rank}(\boldsymbol{A}_{\boldsymbol{X}}^{(k)}) \leq (k+1)d. \tag{11}$$

Thus, we have $\rho_k \geq p_k - (k+1)d$, with ρ_k being the number of singular values close to zero for $\boldsymbol{H}^{(k)} \in \mathbb{R}^{n \times p_k}$. This bound indicates that the PCAPass embeddings will be rank-deficient unless $p_k \leq (k+1)d$. However, note that setting $p_k = (k+1)d$ does not guarantee full-rank embeddings, as additional sources of rank deficiency may be present, such as the potential rank deficiency of $\boldsymbol{X}$ itself.

Having established the rank-deficiency of the PCAPass embeddings regardless of the specific compression method used to compute each $\boldsymbol{W}^{(k)}$, we now examine the PCA compression utilized by Sadowski et al. (2022) in greater detail. Recall that PCA is typically and efficiently implemented through centring and SVD (Murphy, 2012, Ch. 12.2.3). Therefore, if all singular dimensions are retained, the final PCAPass embeddings can be expressed as $\boldsymbol{Z} = \begin{bmatrix}\boldsymbol{U\Sigma} & \boldsymbol{\Upsilon\Sigma}_{\approx 0}\end{bmatrix}$ Here, $\boldsymbol{U\Sigma} \in \mathbb{R}^{n \times (k+1)d}$ represents the informative part of the embeddings, while $\boldsymbol{\Upsilon\Sigma}_{\approx 0} \in \mathbb{R}^{n \times \rho_k}$ captures the singular dimensions, with elements in $\boldsymbol{\Sigma}_{\approx 0}$ being close to zero.

Applying compression in each iteration has the potential to address the rank deficiency by removing the singular dimensions $\boldsymbol{\Upsilon}$. However, the effectiveness of this approach depends on the specifics of the PCA compression. Sadowski et al. (2022) implement a maximum embedding dimension, $p_{\max}$, such that $p_k = \min(p_{\max}, 2^k d)$, where $2^k d$ is the embedding dimension without compression for undirected message-passing. This implies that the PCAPass embedding will remain rank-deficient in each iteration until $(k+1)d \geq p_{\max}$. Thus, using a fixed value for $p_{\max}$ does not ensure the removal of singular dimensions. Instead, the number of retained dimensions would need to vary with each iteration k to guarantee the elimination of all singular dimensions. This introduces additional algorithmic complexity, especially since the bound on p_k must be adapted for directed message-passing and for message-passing with multiple aggregation operations (Jin et al., 2019; Corso et al., 2020).

An alternative approach is to apply a threshold to the singular values during compression, removing any dimensions where $\Sigma_{i,i} \leq \theta \Sigma_{1,1}$, where $\Sigma_{1,1}$ is the largest singular value and $\theta \in [0, 1]$ a relative tolerance. However, setting θ either too low or too high can lead to a loss of accuracy in downstream tasks, see Section 5.1.

Moreover, even if the singular dimensions are successfully eliminated, computational resources have still been unnecessarily spent on computing the redundant features in the first place. Given that the number of singular dimensions can grow rapidly, as suggested by the bound $\rho_k \geq (2^k - k - 1)d$, and that PCA compression has quadratic time complexity with respect to the number of features (Golub & Van Loan, 2013, Ch. 2.4), the amount of unnecessary computation is substantial.

3.3 The negative effects of rank-deficient embeddings on clustering

Rank-deficient or otherwise ill-conditioned embedding matrices can violate fundamental assumptions made by downstream machine learning models, like the linear independence of features, and contribute to the instability of numerical computations (Trefethen & Bau, 1997, Pt. 3). In supervised learning, the adverse effects of rank deficiency are often mitigated through regularization techniques. For example, ridge regression (Hoerl & Kennard, 1970) effectively addresses this issue. However, regularization and model selection become much more challenging in unsupervised settings, where the absence of a guiding supervision signal complicates the process (Ma et al., 2023). As a result, unsupervised tasks that rely on embedding distances, such as clustering and graph alignment, are particularly vulnerable to the negative impacts of rank deficiency.

The rank-deficient embedding matrices produced by PCAPass are especially problematic when subjected to common preprocessing operations like standardization (Aggarwal, 2015, Ch. 2.3.3) and whitening (Hyvärinen et al., 2009). We illustrate this with a simple clustering example. We generate a matrix $\boldsymbol{X} \in \mathbb{R}^{200 \times 6}$, consisting of 200 six-dimensional samples. The data is divided into six classes, each corresponding to a normal distribution centred at one of six equidistant points. This setup ensures that samples from each Gaussian blob are well-separated. We visualize this in Figure 2a using 2D UMAP projections (McInnes et al., 2018).

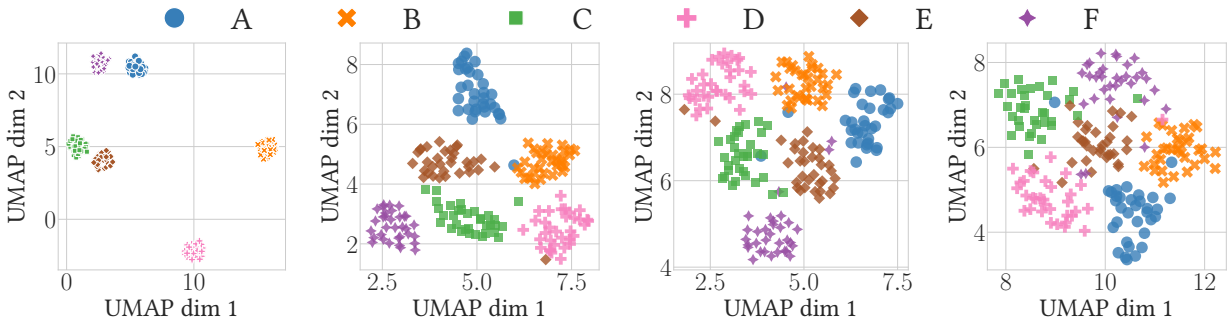

(a) Original, $\boldsymbol{X}$ (b) $\boldsymbol{X}$ duplicated 1 time (c) $\boldsymbol{X}$ duplicated 2 times (d) $\boldsymbol{X}$ duplicated 4 times

Figure 2: The effect of increasing rank deficiency on cluster structures. Figure 2a shows UMAP projection of $\boldsymbol{X}$, comprising 200 data points from 6 classes originally sampled on the surface of a 6D sphere. Figures 2a to 2d illustrate the cluster structure deterioration as $\boldsymbol{X}$ is horizontally concatenated with itself and whitened.

To simulate the introduction of redundant features, we concatenate $\boldsymbol{X}$ with itself, forming $\tilde{\boldsymbol{X}} = \begin{bmatrix}\boldsymbol{X} & \boldsymbol{X}\end{bmatrix}$. Applying PCA-based whitening to $\tilde{\boldsymbol{X}}$ yields the simulated embedding matrix $\boldsymbol{Z} = \sqrt{n-1}\begin{bmatrix}\boldsymbol{U} & \boldsymbol{\Upsilon}\end{bmatrix}$. This expression highlights the connection to PCAPass embeddings that have been standardized to unit variance.

Figure 2 visually demonstrates how cluster separability diminishes as the number of duplicate features increases. This degradation in separability can also be quantified by running k-means clustering (Arthur & Vassilvitskii, 2007). The average normalized mutual information (NMI) (Danon et al., 2005) over 10 seeds is 1.0 for the original data, indicating perfect separation of the classes. However, as $\boldsymbol{X}$ is duplicated, the NMI decreases to 0.78, and then to 0.71 with two duplicates, and down to 0.47 with four duplicates.

Note that the information required to distinguish the clusters remains present in $\boldsymbol{Z}$, and a regularized supervised classifier could still achieve high classification accuracy. However, the relevant information has been diluted by the singular dimensions, $\boldsymbol{\Upsilon}$, which significantly impairs the class's clustering separability.

In this toy example, the negative effects of the singular dimensions can be mitigated by using $\boldsymbol{Z} = \begin{bmatrix}\boldsymbol{U}\boldsymbol{\Sigma} & \boldsymbol{\Upsilon}\boldsymbol{\Sigma}_{\approx 0}\end{bmatrix}$ as input for clustering, which simulates not preprocessing the PCAPass embeddings. However, in practice, preprocessing is often necessary for achieving high task accuracy. Embedding-based graph alignment using structural input features is one such example.

3.4 The negative effects of rank-deficient embeddings on graph alignment

Graph alignment is the task of finding node correspondences between two graphs, $\mathcal{G}_1 = (\mathbb{N}, \mathbb{M}_1)$ and $\mathcal{G}_2 = (\mathbb{N}, \mathbb{M}_2)$. We assume, for simplicity, that while the node set $\mathbb{N}$ is shared, while the edge sets differ. When $\mathbb{M}_2$ is a subset or superset of $\mathbb{M}_1$, we refer to the missing or added edges as noise edges.

Embedding-based graph alignment (Heimann et al., 2018) is a greedy approach where node embeddings are used to match the nodes. Specifically, the nodes in $\mathcal{G}_2$ are matched to the nodes in $\mathcal{G}_1$ with the most similar embeddings in terms of Euclidean distance, which can be computed efficiently using KD-trees (Bentley, 1975). When the graphs lack node attributes, *structural node embeddings* are used (Jin et al., 2021). These embeddings can be generated by message-passing models where $\boldsymbol{X}$ consists of structural features such as node degrees and local clustering coefficients (Fagiolo, 2007).

For this approach to be effective, the embeddings need to be whitened before matching. This is detrimental to the alignment accuracy of PCAPass embeddings, since applying whitening removes the scaling of $\boldsymbol{\Sigma}_{\approx 0}$ from the singular dimensions, allowing $\boldsymbol{\Upsilon}$ to introduce noise into the distance computation. Consequently, the PCAPass embeddings struggle to produce high graph alignment accuracies, as we demonstrate in Section 5.

Figure 3 provides a visual explanation for why whitening is necessary. The gray scatter points in Figure 3a represent the embeddings for each node in $\mathcal{G}_1$, and the ellipse highlights variations along the principal axes of the embedding matrix. The coloured points show a magnified version of the alignment process. The blue circle represents an embedding vector in $\mathcal{G}_1$, and the blue plus represents the corresponding node in $\mathcal{G}_2$. The orange squares represent embeddings for other nodes in $\mathcal{G}_1$.

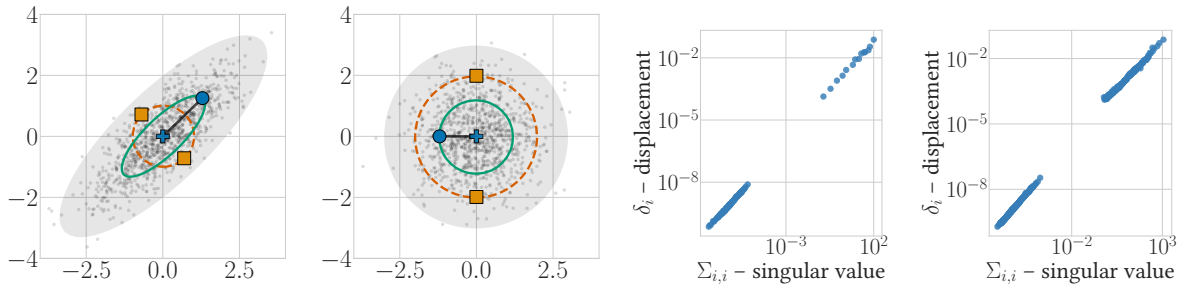

(a) No whitening (b) With whitening (c) Arenas (d) Enron

Figure 3: Visualization explaining the need for whitening in embedding-based graph alignment. In Figure 3a, the goal is to match the blue plus with the blue circle. However, the Euclidean distance fails to account for the data's shape, causing the erroneous orange squares to appear closer. Whitening corrects this issue, as shown in Figure 3b. The assumption in Figure 3a is that the direction of displacement aligns with the data's variation. Figures 3c and 3d provide empirical evidence of a strong correlation between the displacement along axis i and the corresponding singular value, $\Sigma_{i,i}$, based on PCAPass embeddings.

As shown, both orange squares are closer to the blue plus than the blue circle in terms of Euclidean distance. Thus, this node would be incorrectly matched. However, if the covariance of the data is considered in the distance calculation, the blue plus is closer to the blue circle, as indicated by the green ellipse. Whitening spheres the data, equalizing the variance along each principal axis. Therefore, Euclidean distance provides the correct matching in the whitened space, as shown in Figure 3b.

This explanation assumes that the direction of the embedding displacement, indicated by the black arrow in Figure 3a, correlates with the data variation. Figures 3c and 3d provide empirical support for this assumption. These figures show the singular values of the PCAPass embeddings for $\mathcal{G}_1$, denoted $\boldsymbol{Z}^{(1)}$, on the x-axes. The y-axes show the average embedding displacement along the corresponding principal axis, defined as $\delta_i = \frac{1}{n}\|(\boldsymbol{Z}^{(1)} - \boldsymbol{Z}^{(2)})\boldsymbol{V}_{:,i}\|_2$, where $\boldsymbol{V}$ is a basis for the principal axes of $\boldsymbol{Z}^{(1)}$. As seen, the correlation between the directions of variation and displacement is strong, supporting our assumption.

In summary, the rank-deficient embeddings produced by PCAPass contain arbitrary column vectors that act as noise for unsupervised downstream tasks such as clustering and graph alignment. This issue is particularly problematic when normalizing preprocessing steps are required for optimal performance, as is the case with whitening for graph alignment. Therefore, it is crucial to avoid rank-deficient node embeddings.

4 The ACC model and message aggregation

To address the issues of rank-deficient embeddings, we introduce the ACC, which stands for **A**ggregate, **C**ompress, and **C**oncatenate. Performed in this order, these operations result in a message-passing approach where the message matrices, rather than the embeddings, are passed between message-passing iterations. We refer to this as *message aggregation*, and as we will demonstrate, it avoids computing the redundant features that cause the rank deficiency observed in PCAPass. Furthermore, ACC is designed to work with directed graphs, expanding its applicability and versatility.

The complete ACC algorithm is detailed in pseudocode in Algorithm 1. Initially, the feature matrix $\boldsymbol{X}$ is compressed into a c-dimensional message matrix, $\boldsymbol{M}^{(0)} \in \mathbb{R}^{n\times c}$, using Principal Component Analysis (PCA) (Murphy, 2012, Ch. 12.2). Once this initial compression is complete, the message-passing procedure begins. The main distinguishing feature of ACC, as shown on Line 6 of Algorithm 1, is *message aggregation*. This means that ACC applies aggregation operators directly to the message matrices from the previous iteration, $\boldsymbol{M}^{(k)} = \begin{bmatrix}\boldsymbol{A}_{\mathrm{F}}\boldsymbol{M}^{(k-1)} & \boldsymbol{A}_{\mathrm{B}}\boldsymbol{M}^{(k-1)}\end{bmatrix}$. This approach is crucial for avoiding the creation of redundant features, as seen in PCAPass when aggregating and concatenating embedding matrices in Equation 9.

The new message matrix $\boldsymbol{M}^{(k)}$ is then compressed to c dimensions using PCA and concatenated with the embedding matrix, $\boldsymbol{H}^{(k)} = \begin{bmatrix}\boldsymbol{H}^{(k-1)} & \boldsymbol{M}^{(k)}\end{bmatrix}$. Consequently, the final embedding matrix is a concatenation of all message matrices, $\boldsymbol{H}^{(K)} = \begin{bmatrix}\boldsymbol{M}^{(0)} & \boldsymbol{M}^{(1)} \dots & \boldsymbol{M}^{(K)}\end{bmatrix}$, with a total embedding dimension of $p = (K+1)c$.

Algorithm 1: The ACC algorithm for a directed graph $\mathcal{G}$ with node features $\boldsymbol{X}$ using K message-passing iterations, desired dimensionality $p_{\max}$, minimal message size $c_{\min}$ and relative tolerance $\theta \in [0, 1]$.

1 **def** ACC($\mathcal{G}$, $\boldsymbol{X}$, K, $p_{\max}$, $c_{\min} = 2$, $\theta = 10^{-8}$):
2 $\quad c = \max\left(\lfloor p_{\max}/(K+1) \rfloor, c_{\min}\right)$
3 $\quad \boldsymbol{M}^{(0)} = \texttt{PCA}(\boldsymbol{X}, c, \theta)$
4 $\quad \boldsymbol{H}^{(0)} = \boldsymbol{M}^{(0)}$
5 $\quad$ **for** k **in** range$(1, K+1)$:
$\quad\quad$ # Compute aggregations in both direction.
6 $\quad\quad \boldsymbol{M}^{(k)} = \left[\boldsymbol{A}_{\mathtt{F}}\boldsymbol{M}^{(k-1)} \quad \boldsymbol{A}_{\mathtt{B}}\boldsymbol{M}^{(k-1)}\right]$
7 $\quad\quad \boldsymbol{M}^{(k)} \leftarrow \texttt{PCA}(\boldsymbol{M}^{(k)}, c, \theta)$
$\quad\quad$ # Concatenate with existing embeddings.
8 $\quad\quad \boldsymbol{H}^{(k)} = \left[\boldsymbol{H}^{(k-1)} \quad \boldsymbol{M}^{(k)}\right]$
9 $\quad$ **return** $\boldsymbol{H}^{(K)}$

Algorithm 2: PCA compression computed via SVD as used for ACC. Here $\boldsymbol{X} \in \mathbb{R}^{n \times p}$ is a real-valued matrix, c an integer s.t. $c \leq p$, and $\theta \in [0, 1]$ a relative tolerance.

1 **def** PCA($\boldsymbol{X}$, c, θ):
2 $\quad \boldsymbol{X} \leftarrow \texttt{centre_columns}(\boldsymbol{X})$
3 $\quad \boldsymbol{U}, \boldsymbol{\Sigma}, \boldsymbol{V}^{\intercal} = \texttt{SVD}(\boldsymbol{X})$
$\quad$ # Find the index of the smallest singular value which exceeds the given tolerance relative to the largest singular value $\Sigma_{1,1}$.
4 $\quad k_\theta = \max\{j \mid \Sigma_{j,j} \geq \theta\Sigma_{1,1}\}$
$\quad$ # Keep at most k_θ dimensions.
5 $\quad k = \min(c, k_\theta)$
6 $\quad \boldsymbol{X}_c = \boldsymbol{X}\boldsymbol{V}_{:,:k}$
7 $\quad$ **return** $\boldsymbol{X}_c$

Typically, the value of c is chosen as the largest integer such that the total embedding dimension p does not exceed a desired limit, $(K+1)c \leq p_{\max}$. However, this condition would result in $c = 0$ if $(K+1) > p_{\max}$. To prevent this, ACC enforces a minimal value for c, denoted as $c_{\min}$, as specified on Line 2 of Algorithm 1. By default, we set $c_{\min} = 2$ to account for the two message-passing directions in directed graphs.

For undirected graphs, ACC is slightly modified on Line 6, as message-passing is conducted using only the undirected matrix $\boldsymbol{A}_{\mathtt{N}}$, $\boldsymbol{M}^{(k)} = \boldsymbol{A}_{\mathtt{N}}\boldsymbol{M}^{(k-1)}$. In this scenario, the compression steps on Line 7 is technically unnecessary since $\boldsymbol{M}^{(k)}$ is already c-dimensional. Nonetheless, for consistency across our experiments, we always perform PCA.

To demonstrate that ACC avoids computing the redundant features seen for PCAPass in Equation 9, we write out the expression for the undirected ACC embeddings after K iterations: $\boldsymbol{H}^{(K)} = \left[\boldsymbol{X}\boldsymbol{W}^{(0)}, \boldsymbol{A}_{\mathtt{N}}\boldsymbol{X}\boldsymbol{W}^{(1)}, \ldots, \boldsymbol{A}_{\mathtt{N}}^{K}\boldsymbol{X}\boldsymbol{W}^{(K)}\right]$. In this formulation, each $\boldsymbol{W}^{(k)} \in \mathbb{R}^{d \times c}$ is a compression matrix derived from successive applications of PCA. Unlike PCAPass, the ACC embeddings exclude the repeated submatrices found in Equation 9. Specifically, $\boldsymbol{H}^{(K)}$ in ACC contains exactly one instance of $\boldsymbol{A}_{\mathtt{N}}^{k}\boldsymbol{X}$ for each $k \in \{0, \ldots, K\}$, representing the non-redundant information produced at each iteration.

We can further verify that the ACC embeddings are not rank-deficient by examining the number of singular values close to zero, denoted as ρ_K, where K represents the number of message-passing iterations. To compute ρ_K, we count the number of singular values for which $\Sigma_{ii} \leq 10^{-6}\Sigma_{11}$. Figure 4 illustrates ρ_K for both the ACC and PCAPass embeddings, along with the corresponding embedding dimensions p_K, for two graphs: Arenas, an undirected graph, and Enron, a directed graph. The initial number of features is $d = 2$ for Arenas and $d = 6$ for Enron. In both cases, the maximum embedding dimensionality $p_{\max} = 512$ is applied.

We observe that the number of small singular values remains at zero for all values of K for ACC, indicating that its embeddings are full rank. In contrast, for PCAPass, ρ_K grows rapidly for both graphs until the embedding dimensionality p_K reaches the maximum value $p_{\max}$. For Arenas, the growth of ρ_K closely follows our predicted lower bound $(2^k - k - 1)d$, as depicted by the dashed black curve in Figure 4a. For Enron, ρ_K initially increases more rapidly than for Arenas, consistent with the fact that the dimensionality p_K expands more quickly for directed graphs due to the concatenation of forward and backward aggregations. This also results in $p_{\max}$ being reached sooner, and as a consequence, the singular dimensions are replaced by non-redundant features after $K = 4$, causing ρ_K to drop to zero. This analysis highlights the interaction between the PCAPass rank deficiency, the number of message-passing iterations, and the maximum dimensionality used for PCA compression.

While message aggregation effectively avoids computing the redundant features highlighted for PCAPass in Equation 8, other sources of singular dimensions can still arise. For instance, singular dimensions can be introduced if $\boldsymbol{X}$ itself is not full rank, or if the adjacency matrix contains eigenvalues close to zero. To mitigate these issues, ACC employs a small threshold θ during the PCA compression to discard embedding dimensions with small singular values, as outlined in Lines 4 to 6 of Algorithm 2.

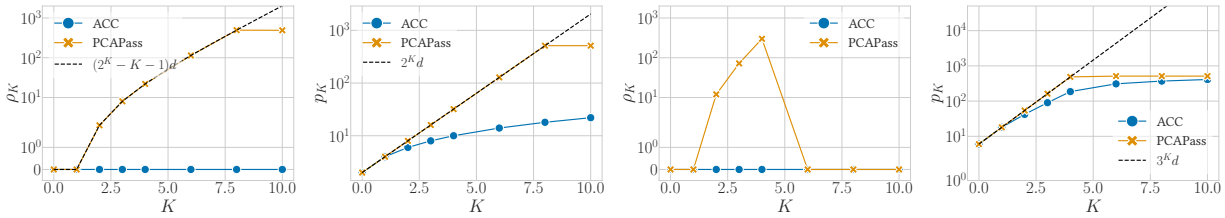

(a) Arenas, # $\Sigma_{i,i} \approx 0$ (b) Arenas, dimensions (c) Enron, # $\Sigma_{i,i} \approx 0$ (d) Enron, dimensions

Figure 4: Figures 4a and 4c show the number of small singular values, ρ_K, as a function of the number of message-passing iterations, K, for two graphs: Arenas and Enron. The dashed line in 4a represents the theoretical prediction for ρ_K discussed in Section 3.2. Figures 4b and 4d display the embedding dimensionality p_K. Both ACC and PCAPass use the maximum dimensionality $p_{\max} = 512$, resulting in the curve cut-off.

However, singular dimensions can also emerge due to correlations across message-passing iterations. For example, if $\boldsymbol{X}$ contains an eigenvector of $\boldsymbol{A}_{\mathtt{N}}$, this would introduce a singular dimension in $\begin{bmatrix}\boldsymbol{X} & \boldsymbol{A}_{\mathtt{N}}\boldsymbol{X}\end{bmatrix}$. ACC cannot remove these correlations during message-passing because the messages from each iteration are compressed independently. This further implies that the dimensions of the final ACC embeddings, $\boldsymbol{Z}$, may exhibit correlations, which could impact certain downstream tasks.

To address these concerns, decorrelation and removal of singular dimensions from $\boldsymbol{H}^{(K)}$ after message-passing could be beneficial. However, in our experiments, we have not incorporated these steps by default, treating them instead as potential preprocessing steps for specific downstream tasks.

4.1 Time complexity, scalability, and the inductive learning setting

The time complexity of ACC is primarily determined by the message aggregation and PCA compression steps (lines 3, 6, and 7 in Algorithm 1). For an input matrix of size $n \times p$, PCA has a complexity of $\mathcal{O}(np^2)$, which follows from both the time complexity of SVD (Golub & Van Loan, 2013, Ch. 5.5.6) and the matrix multiplication on line 6 of Algorithm 2. The message aggregation step consists of sparse-dense matrix multiplications, which have a complexity of $\mathcal{O}(mc)$. Thus, the overall time complexity of ACC is $\mathcal{O}(nd^2 + Kmc + Knc^2)$.

The linear dependence on n and m highlights the scalability of ACC. Moreover, both the message aggregation and PCA computations benefit from parallelization and GPU acceleration, as supported by prevalent graph learning libraries (Paszke et al., 2019; Fey & Lenssen, 2019). Notably, ACC learns embeddings in a single forward pass, without requiring gradient-based optimization. This contrasts with self-supervised graph neural networks, which typically require hundreds or even thousands of training epochs (Hou et al., 2022), making ACC a computationally efficient alternative.

ACC is primarily designed for transductive learning, where the entire graph is available during training, and its efficiency allows for straightforward recomputation of embeddings when the graph is updated. However, ACC can also be extended to inductive settings using a GraphSAGE-inspired approach (Hamilton et al., 2017). Given a new node with known features and connections to existing nodes, its embedding can be computed by aggregating messages from its neighbours within a sampled subgraph.

The main challenge in the inductive setting lies in the PCA-based compression step, as the projection matrices $\boldsymbol{V}^{(k)}$ are derived from the training graph. A natural solution is to project new message matrices $\boldsymbol{M}^{(k)}$ onto the existing PCA bases in each iteration, ensuring consistency with previously learned embeddings. Additionally, incremental PCA techniques could be employed to update the basis dynamically without requiring full recomputation (Balsubramani et al., 2013; Yu et al., 2017).

Both subgraph sampling and incremental PCA introduce potential sources of noise in the embedding process, necessitating careful empirical evaluation. However, given the efficiency of ACC, inductive extensions are primarily relevant for massive graphs, and we leave their detailed study to future work.

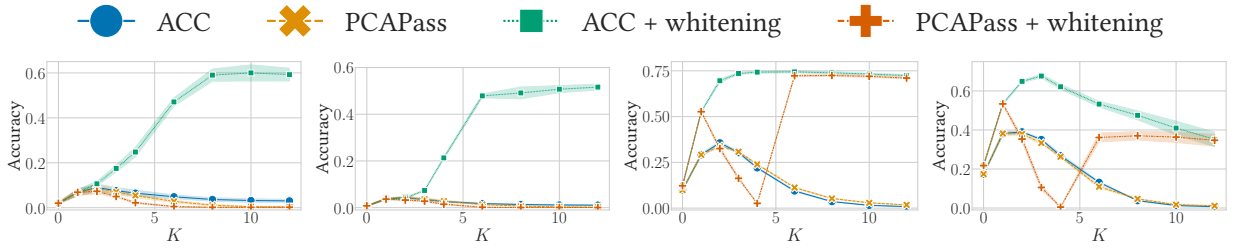

(a) Arenas (b) PPI (c) Enron (d) Polblogs

Figure 5: ACC and PCAPass for graph alignment with 15% noise edges. The x-axis shows the number of message-passing iterations K. Markers and shaded areas represent the average and standard deviation over 5 seeds. Without whitening, both algorithms perform poorly. Whitening benefits ACC across all datasets, with its accuracy reaching 60% on Arenas compared to 10% for PCAPass. Whitening only benefits PCAPass when embeddings are not rank-deficient, as shown in figure 4.

5 Experiments

In this section, we empirically demonstrate the superior graph alignment accuracy of the ACC model compared to PCAPass, highlighting the negative impact of rank deficiency. Additionally, we compare ACC to state-of-the-art self-supervised graph neural networks (SSGNNs) across five standard node classification benchmarks for directed graphs (Rossi et al., 2023). Our results show that ACC is over 70 times faster on the largest datasets while achieving better accuracy with default hyperparameters compared to the SSGNNs.

5.1 Graph alignment: ACC vs. PCAPass

For evaluating alignment accuracy, we use established protocols from Heimann et al. (2018). Specifically, we create a second graph $\mathcal{G}_2$ from a reference graph $\mathcal{G}_1$ by permuting node indices and removing 15% of the edges. We use four graphs with this setup: Arenas, PPI, Enron, and Polblogs. Arenas and PPI are well-known benchmark graphs (Heimann et al., 2018; Jin et al., 2021; Skitsas et al., 2023), while Enron and Polblogs provide examples of directed graphs.

In addition, we assess performance on the real-world Magna dataset (Saraph & Milenković, 2014). In Magna, the noisy graph $\mathcal{G}_2$ includes 15% *more* edges than $\mathcal{G}_1$. These noise edges were selected by Saraph & Milenković (2014) based on observed node interaction probabilities. Real-world datasets like Magna are rare due to the inherent complexity of the graph alignment problem. Detailed statistics about the datasets are provided in Appendix C.1.

For both ACC and PCAPass, we set the maximum embedding dimension to $p_{\max} = 512$ and use node structural features as input, $\boldsymbol{X} \in \mathbb{R}^{n \times d}$. For undirected graphs, the input features are the node's degree and local clustering coefficient, resulting in $d = 2$. For directed graphs, the feature set is expanded to include the in-degree, out-degree, and four local clustering coefficients, as defined by Fagiolo (2007). These coefficients—*out*, *in*, *cycle*, and *middleman*—correspond to the four unique ways to orient the edges of a directed triangle, giving $d = 6$.

We first compare ACC and PCAPass across varying numbers of message-passing iterations K, both with and without whitening, as shown in Figure 5. Without whitening, both ACC and PCAPass show low accuracies, which is expected given the need for whitening in embedding-based graph alignment, as discussed in Section 3.4. With whitening, ACC's accuracy improves markedly on all datasets, reaching 60% on Arenas and 75% on Enron. In contrast, PCAPass accuracy remains low for undirected graphs, peaking at only 10% on Arenas. For directed graphs, accuracy initially improves, then deteriorates, and eventually increases again. This fluctuation is closely linked to the number of singular dimensions in PCAPass embeddings. As shown in Figure 4c, accuracy drops during periods when the number of small singular values is high, particularly for $K \in \{2, 3, 4\}$. These results highlight the detrimental effect of rank deficiency on alignment accuracy.

We next examine how singular value thresholding can address the rank deficiency in PCAPass. Specifically, we apply a threshold θ such that dimensions with singular values $\Sigma_{i,i} \leq \theta \Sigma_{1,1}$ are removed, where $\Sigma_{1,1}$ is the largest singular value. For this experiment, we use $K = 10$ for undirected graphs and $K = 4$ for directed graphs, as these settings exhibit the maximum rank deficiency for PCAPass.

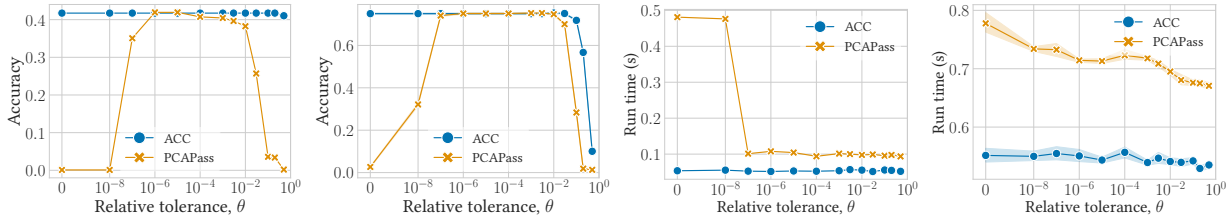

(a) Magna, accuracy (b) Enron, accuracy (c) Magna, run time (d) Enron, run time

Figure 6: ACC and PCAPass for graph alignment with 15% noise edges, $K = 10$ for Magna, and $K = 4$ for Enron. The x-axes show the relative tolerance θ used to remove dimensions with small singular values. Figures 6a and 6b show accuracy on the y-axis, while 6c and 6d show run time. Markers and shaded areas indicate the average and standard deviation over 5 seeds. ACC achieves equal or superior accuracy for all θ, and retains its accuracy for $\theta = 0$, as its embeddings are full rank. ACC is also consistently faster than PCAPass.

The results are presented in Figure 6, with the threshold θ varying along the x-axis. We see that selecting an appropriate θ can resolve the rank deficiency, allowing PCAPass to achieve accuracies comparable to ACC. However, θ must be carefully chosen: it needs to be high enough to remove singular dimensions effectively, but not so high that it eliminates necessary dimensions. The favourable θ range depends on numerical precision and dataset characteristics; for Magna, only $\theta \in [10^{-6}, 10^{-5}]$ yields accuracies matching ACC.

Additionally, ACC consistently outperforms PCAPass in terms of speed by avoiding computation of redundant features. As illustrated in Figure 6c and 6d, the relative reduction in run time can be substantial. For instance, on the Magna dataset, ACC is 80% faster than PCAPass, with a run time around 55 ms compared to 100 ms for PCAPass.

5.2 Node classification: ACC vs self-supervised graph neural networks

To compare ACC with self-supervised graph neural networks (SSGNNs), we evaluate node classification accuracy on five standard directed graph datasets from the literature (Pei et al., 2020; Lim et al., 2021; Platonov et al., 2023; Rossi et al., 2023). Dataset details are provided in Appendix C.1. For initial node features $\boldsymbol{X}$, we use both the dataset-provided node features and the structural features used for graph alignment.

We train a gradient boosting classifier on top of the embeddings, following the setup of Sadowski et al. (2022). Specifically, we employ Scikit-learn's implementation of LightGBM (Ke et al., 2017) with default hyperparameters. To ensure robustness, we perform three repeats of 5-fold cross-validation with five different random seeds, reporting mean and standard deviation statistics for the classification accuracy.

All models are executed in a Google Cloud g2-standard-32 environment with one Nvidia L4 24GB GPU, 32 vCPUs @ 2.20GHz, and 128 GB of memory. Reported run times are averages over the five random seeds.

We adapt all baseline models to use directed message-passing following the approach outlined by Rossi et al. (2023), except for MVGRL (Hassani & Khasahmadi, 2020) and GREET (Liu et al., 2023), which feature non-standard architectures. Additionally, we introduce BGRL-GS and GraphMAEv2-GS by replacing the default GNNs in BGRL (Thakoor et al., 2022) and GraphMAEv2 (Hou et al., 2023) with the GraphSAGE model (Hamilton et al., 2017). SGCN and PCAPass are also included in our comparisons. For all models, including ACC, we use $K = 2$ message-passing iterations and $p = 512$ embedding dimensions, both of which are commonly used values in the literature (Hamilton et al., 2017; Veličković et al., 2018; Zhang et al., 2021; Thakoor et al., 2022; Hou et al., 2022). We use default values for optimizer and loss function hyperparameters.

Note that the goal of this experiment is to evaluate the expected quality of the unsupervised embeddings in real-world scenarios where ground-truth label information cannot be expected to be available. Therefore, we do not perform any model hyperparameter tuning, as identifying optimal hyperparameter configuration without access to ground-truth validation data is highly challenging (Ma et al., 2023). As a result, evaluating models with default settings offers a more practical and realistic assessment of their performance in real-world unsupervised embedding scenarios. However, we nevertheless acknowledge the larger expressive power of GNNs compared to ACC, meaning that there no doubt exists dataset specific hyperparameter settings where the GNN embeddings result in higher classification accuracy than ACC.

Table 1: Gradient boosting node classification results. The top 3 accuracies are highlighted in bold. Snap Patents results were gathered using CPU only due to GPU memory limits. OOM abbreviates *out of memory*.

Model	Chameleon		Squirrel		Roman Empire		Arxiv Year		Snap-Patents	
	Accuracy	Time	Accuracy	Time	Accuracy	Time	Accuracy	Time	Accuracy	Time
No model, $\mathbf{X}$	64.6 ± 2.3	0ms	52.1 ± 1.4	0ms	70.4 ± 0.7	0ms	44.7 ± 0.2	0ms	56.1 ± 0.1	0ms
GAE[1]	62.2 ± 2.2	11s	44.8 ± 1.5	1m 4s	53.4 ± 3.1	16s	42.3 ± 0.3	7m 34s	51.9 ± 0.1	3h 15m
DGI[2]	61.5 ± 2.3	14s	44.2 ± 1.6	1m 40s	73.4 ± 0.9	4m 2s	$\mathbf{47.1 \pm 0.2}$	5h	Timeout	≥24h
MVGRL[3]	66.3 ± 2.2	26m 44s	46.4 ± 1.5	26m 32s	64.3 ± 1.0	39m 13s	OOM	≥128 GB	OOM	≥128 GB
BGRL[4]	66.1 ± 2.2	7m 49s	46.7 ± 1.3	31m 45s	76.0 ± 0.8	25m 24s	46.6 ± 0.3	4h 52m	Timeout	≥24h
BGRL-GS[4]	65.3 ± 2.2	8m 31s	44.8 ± 1.5	33m 21s	74.4 ± 0.7	21m 52s	43.7 ± 0.2	3h 8m	Timeout	≥24h
CCA-SSG[5]	71.0 ± 2.1	4s	$\mathbf{59.9 \pm 1.2}$	7s	63.7 ± 0.7	10s	$\mathbf{48.4 \pm 0.2}$	1m 11s	$\mathbf{56.1 \pm 0.0}$	1h 40m
GraphMAE[6]	68.9 ± 2.0	27s	56.9 ± 1.8	59s	53.9 ± 1.0	1m 8s	44.2 ± 0.3	8m 55s	45.6 ± 0.1	16h
GraphMAEv2[7]	69.6 ± 1.9	36s	51.2 ± 2.5	1m 14s	53.5 ± 0.9	1m 46s	44.3 ± 0.3	14m 53s	44.0 ± 0.0	23h
GraphMAEv2-GS[7]	$\mathbf{74.1 \pm 2.3}$	29s	57.0 ± 1.4	1m 6s	$\mathbf{80.0 \pm 0.7}$	1m 35s	46.3 ± 0.3	10m 46s	53.8 ± 0.1	18h
GREET[8]	61.4 ± 2.2	1m 25s	44.2 ± 1.6	6m 45s	$\mathbf{80.1 \pm 0.5}$	1h 56m	OOM	≥128 GB	OOM	≥128 GB
SPGCL[9]	66.3 ± 2.2	16s	45.8 ± 1.5	1m 23s	73.6 ± 0.8	55s	46.4 ± 0.2	52m 6s	OOM	≥128 GB
SGCN[10]	$\mathbf{74.7 \pm 1.8}$	374ms	$\mathbf{68.3 \pm 1.4}$	723ms	45.4 ± 0.8	393ms	45.0 ± 0.2	1s	50.2 ± 0.1	26s
PCAPass[11]	71.7 ± 2.2	2s	51.5 ± 1.3	22s	73.0 ± 0.7	852ms	46.3 ± 0.2	2s	$\mathbf{61.2 \pm 0.1}$	2m 20s
ACC	$\mathbf{76.6 \pm 1.9}$	1s	$\mathbf{71.5 \pm 1.3}$	1s	$\mathbf{81.5 \pm 0.6}$	432ms	$\mathbf{49.4 \pm 0.3}$	1s	$\mathbf{62.6 \pm 0.1}$	27s

[1] Kipf & Welling (2017) [2] Veličković et al. (2019) [3] Hassani & Khasahmadi (2020) [4] Thakoor et al. (2022) [5] Zhang et al. (2021) [6] Hou et al. (2022) [7] Hou et al. (2023) [8] Liu et al. (2023) [9] Wang et al. (2023) [10] Wu et al. (2019) [11] Sadowski et al. (2022)

Table 1 displays the accuracies and run times for all models and datasets. ACC stands out with the highest accuracy across all datasets. Moreover, these results demonstrate ACC's superior scalability compared to SSGNNs. On the Arxiv Year dataset, with 1 milion edges, ACC is over 70 times faster than CCA-SSG, the fastest SSGNN. Moreover, whereas most SSGNNs take a full day or more to run on Snap Patents, the largest dataset with 14 million edges, ACC requires *only 27 seconds*.

The linear model SGCN is the only baseline faster than ACC. However, SGCN suffers from over-smoothing, leading to ACC's substantial accuracy advantage on the Roman Empire dataset. This underscores how ACC's concatenation approach mitigates over-smoothing. Further results are available in the Appendix D.

Additionally, we observe a significant accuracy discrepancy between ACC and PCAPass on the Squirrel dataset, which cannot be attributed to the PCAPass rank deficiency. Our detailed analysis, available in Appendix E, highlights another benefit of ACC's message aggregation. Unlike PCAPass, which compresses its full embeddings in each iteration and may discard informative but low-variance features, ACC compresses features separately at each iteration, preserving information more evenly. Consequently, the ACC embeddings retains more information than PCAPass from the class-informative but low-variance features provided by $\boldsymbol{A}_{\text{B}}\boldsymbol{X}$ in the Squirrel dataset, resulting in higher accuracy.

6 Conclusion and future work

In this paper, we addressed the issue of rank-deficient node embeddings generated by message-passing models, which not only inefficient but also risk degrading downstream task performance. To overcome this, we introduced ACC, a novel unsupervised node embedding model that leverages message aggregation to avoid redundant feature computation, ensuring that the resulting embeddings are full rank.

A promising avenue for future research is to investigate whether ACC's PCA-based compression can be framed as the optimization of a model-wide loss function. Such a formulation could deepen our understanding of ACC and provide insights that may benefit the broader field of unsupervised message-passing models.

Additionally, ACC's message aggregation approach ensures that each embedding feature is tied to a specific number of hops in the graph. Replacing PCA with a feature selection algorithm could further enhance interpretability by associating each embedding feature with a single input feature. This extension could be particularly valuable for applications requiring model transparency, such as anomaly detection.

References

Lada A. Adamic and Natalie Glance. The Political Blogosphere and the 2004 U.S. Election: Divided They Blog. In *LinkKDD '05*, pp. 36–43, 2005. URL https://doi.org/10.1145/1134271.1134277.

Charu C. Aggarwal. *Data Mining: The Textbook*. Springer, first edition, 2015. URL https://doi.org/10.1007/978-3-319-14142-8.

David Arthur and Sergei Vassilvitskii. K-means++: The Advantages of Careful Seeding. In *SODA '07*, pp. 1027–1035, 2007. URL https://dl.acm.org/doi/10.5555/1283383.1283494.

Akshay Balsubramani, Sanjoy Dasgupta, and Yoav Freund. The fast convergence of incremental pca. In *NeurIPs '13*, volume 26, 2013. URL https://doi.org/10.48550/arXiv.1501.03796.

Jon Louis Bentley. Multidimensional Binary Search Trees Used for Associative Searching. *Communications of the ACM*, 18(9):509–517, 1975. URL https://doi.org/10.1145/361002.361007.

Bobby-Joe Breitkreutz, Chris Stark, Teresa Reguly, Lorrie Boucher, Ashton Breitkreutz, Michael Livstone, Rose Oughtred, Daniel H. Lackner, Jürg Bähler, Valerie Wood, Kara Dolinski, and Mike Tyers. The BioGRID Interaction Database: 2008 update. *Nucleic Acids Research*, 36(suppl_1):D637–D640, 2007. URL https://doi.org/10.1093/nar/gkm1001.

Shaosheng Cao, Wei Lu, and Qiongkai Xu. Grarep: Learning graph representations with global structural information. In *CIKM '15*, pp. 891–900, 2015. URL https://doi.org/10.1145/2806416.2806512.

Deli Chen, Yankai Lin, Wei Li, Peng Li, Jie Zhou, and Xu Sun. Measuring and Relieving the Over-Smoothing Problem for Graph Neural Networks from the Topological View. *Proceedings of the AAAI Conference on Artificial Intelligence*, 34(04):3438–3445, 2020. URL https://doi.org/10.1609/aaai.v34i04.5747.

Gabriele Corso, Luca Cavalleri, Dominique Beaini, Pietro Liò, and Petar Velickovic. Principal Neighbourhood Aggregation for Graph Nets. In *NeurIPS'20*, 2020. URL https://proceedings.neurips.cc/paper/2020/hash/99cad265a1768cc2dd013f0e740300ae-Abstract.html.

Leon Danon, Albert Díaz-Guilera, Jordi Duch, and Alex Arenas. Comparing community structure identification. *Journal of Statistical Mechanics: Theory and Experiment*, 2005(09), 2005. URL https://dx.doi.org/10.1088/1742-5468/2005/09/P09008.

Claire Donnat, Marinka Zitnik, David Hallac, and Jure Leskovec. Learning Structural Node Embeddings Via Diffusion Wavelets. In *KDD'18*, pp. 1320–1329, 2018. URL https://doi.org/10.1145/3219819.3220025.

Giorgio Fagiolo. Clustering in complex directed networks. *Physical Review E*, 76(2), 2007. URL https://doi.org/10.1103/PhysRevE.76.026107.

Matthias Fey and Jan E. Lenssen. Fast graph representation learning with PyTorch Geometric. In *ICLR Workshop on Representation Learning on Graphs and Manifolds*, 2019. URL https://doi.org/10.48550/arXiv.1903.02428.

Justin Gilmer, Samuel S. Schoenholz, Patrick F. Riley, Oriol Vinyals, and George E. Dahl. Neural Message Passing for Quantum Chemistry. In *ICML '17*, pp. 1263–1272, 2017. URL https://proceedings.mlr.press/v70/gilmer17a.html.

Gene H. Golub and Charles F. Van Loan. *Matrix Computations*. JHU Press, fourth edition, 2013.

Roger Guimera, Leon Danon, Albert Díaz-Guilera, and Francesc Giraltand Alex Arenas. Self-similar community structure in a network of human interactions. *Physical Review E*, 68:065103, 2003. URL https://doi.org/10.1103/PhysRevE.68.065103.

Will Hamilton, Zhitao Ying, and Jure Leskovec. Inductive Representation Learning on Large Graphs. In *NeurIPS'17*, 2017. URL https://doi.org/10.48550/arXiv.1706.02216.

Per Christian Hansen. *Rank-Deficient and Discrete Ill-Posed Problems*. Society for Industrial and Applied Mathematics, 1998. URL https://epubs.siam.org/doi/abs/10.1137/1.9780898719697.

Kaveh Hassani and Amir Hosein Khasahmadi. Contrastive Multi-View Representation Learning on Graphs. In *ICML'20*, pp. 4116–4126, 2020. URL https://proceedings.mlr.press/v119/hassani20a.html.

Mark Heimann, Haoming Shen, Tara Safavi, and Danai Koutra. Regal: Representation Learning-Based Graph Alignment. In *CIKM'18*, pp. 117–126, 2018. URL https://doi.org/10.1145/3269206.3271788.

Keith Henderson, Brian Gallagher, Tina Eliassi-Rad, Hanghang Tong, Sugato Basu, Leman Akoglu, Danai Koutra, Christos Faloutsos, and Lei Li. RolX: structural role extraction & mining in large graphs. In *KDD'12*, pp. 1231–1239. Association for Computing Machinery, 2012. URL https://doi.org/10.1145/2339530.2339723.

Arthur E. Hoerl and Robert W. Kennard. Ridge Regression: Biased Estimation for Nonorthogonal Problems. *Technometrics*, 12(1):55–67, 1970. URL http://www.jstor.org/stable/1267351.

Roger A. Horn and Charles R. Johnson. *Matrix Analysis*. Cambridge University Press, 2 edition, 2012. URL https://doi.org/10.1017/9781139020411.

Zhenyu Hou, Xiao Liu, Yukuo Cen, Yuxiao Dong, Hongxia Yang, Chunjie Wang, and Jie Tang. GraphMAE: Self-Supervised Masked Graph Autoencoders. In *KDD'22*, pp. 594–604, 2022. URL https://doi.org/10.1145/3534678.3539321.

Zhenyu Hou, Yufei He, Yukuo Cen, Xiao Liu, Yuxiao Dong, Evgeny Kharlamov, and Jie Tang. GraphMAE2: A Decoding-Enhanced Masked Self-Supervised Graph Learner. In *WWW'23*, pp. 737–746, 2023. URL https://doi.org/10.1145/3543507.3583379.

Weihua Hu, Matthias Fey, Marinka Zitnik, Yuxiao Dong, Hongyu Ren, Bowen Liu, Michele Catasta, and Jure Leskovec. Open Graph Benchmark: Datasets for Machine Learning on Graphs. In *NeurIPS '20*, pp. 22118–22133, 2020. URL https://doi.org/10.48550/arXiv.2005.00687.

Aapo Hyvärinen, Jarmo Hurri, and Patrik O. Hoyer. *Principal Components and Whitening*, pp. 93–130. Springer London, 2009. URL https://doi.org/10.1007/978-1-84882-491-1_5.

Di Jin, Ryan A. Rossi, Eunyee Koh, Sungchul Kim, Anup Rao, and Danai Koutra. Latent Network Summarization: Bridging Network Embedding and Summarization. In *KDD'19*, pp. 987–997, 2019. URL https://doi.org/10.1145/3292500.3330992.

Junchen Jin, Mark Heimann, Di Jin, and Danai Koutra. Toward Understanding and Evaluating Structural Node Embeddings. *ACM TKDD*, 16(3), 2021. URL https://doi.org/10.1145/3481639.

Guolin Ke, Qi Meng, Thomas Finley, Taifeng Wang, Wei Chen, Weidong Ma, Qiwei Ye, and Tie-Yan Liu. LightGBM: A Highly Efficient Gradient Boosting Decision Tree. In *NeurIPS'17*, pp. 3149–3157, 2017. URL https://dl.acm.org/doi/10.5555/3294996.3295074.

Thomas N. Kipf and Max Welling. Semi-Supervised Classification with Graph Convolutional Networks. In *ICLR '17*, 2017. URL https://openreview.net/pdf?id=SJU4ayYgl.

Bryan Klimt and Yiming Yang. The Enron Corpus: A New Dataset for Email Classification Research. In *Machine Learning: ECML 2004*, pp. 217–226. Springer Berlin Heidelberg, 2004. URL https://doi.org/10.1007/978-3-540-30115-8_22.

Jure Leskovec, Jon Kleinberg, and Christos Faloutsos. Graphs over time: densification laws, shrinking diameters and possible explanations. In *KDD '05*, pp. 177–187, 2005. URL https://doi.org/10.1145/1081870.1081893.

Qimai Li, Zhichao Han, and Xiao-Ming Wu. Deeper Insights Into Graph Convolutional Networks for Semi-Supervised Learning. In *AAAI'18*, 2018. URL https://doi.org/10.1609/aaai.v32i1.11604.

Derek Lim, Felix Matthew Hohne, Xiuyu Li, Sijia Linda Huang, Vaishnavi Gupta, Omkar Prasad Bhalerao, and Ser-Nam Lim. Large Scale Learning on Non-Homophilous Graphs: New Benchmarks and Strong Simple Methods. In *NeurIPS'21*, 2021. URL https://doi.org/10.48550/arXiv.2110.14446.

Yixin Liu, Yizhen Zheng, Daokun Zhang, Vincent Lee, and Shirui Pan. Beyond Smoothing: Unsupervised Graph Representation Learning with Edge Heterophily Discriminating. In *AAAI'23*, pp. 4516–4524, 2023. URL https://doi.org/10.1609/aaai.v37i4.25573.

Martin Q. Ma, Yue Zhao, Xiaorong Zhang, and Leman Akoglu. The Need for Unsupervised Outlier Model Selection: A Review and Evaluation of Internal Evaluation Strategies. *ACM SIGKDD Explorations Newsletter*, 25(1):19–35, 2023. URL https://doi.org/10.1145/3606274.3606277.

Leland McInnes, John Healy, and James Melville. UMAP: Uniform Manifold Approximation and Projection for Dimension Reduction. *ArXiv e-prints*, 2018. URL https://doi.org/10.48550/arXiv.1802.03426.

Kevin P. Murphy. *Machine Learning: A Probabilistic Perspective*. MIT press, 2012. URL https://mitpress.mit.edu/9780262018029/.

Adam Paszke, Sam Gross, Francisco Massa, Adam Lerer, James Bradbury, Gregory Chanan, Trevor Killeen, Zeming Lin, Natalia Gimelshein, Luca Antiga, Alban Desmaison, Andreas Kopf, Edward Yang, Zachary DeVito, Martin Raison, Alykhan Tejani, Sasank Chilamkurthy, Benoit Steiner, Lu Fang, Junjie Bai, and Soumith Chintala. PyTorch: An Imperative Style, High-Performance Deep Learning Library. In *NeurIPs '19*, pp. 8024–8035, 2019. URL https://dl.acm.org./doi/10.5555/3454287.3455008.

Hongbin Pei, Bingzhe Wei, Kevin Chen-Chuan Chang, Yu Lei, and Bo Yang. Geom-GCN: Geometric Graph Convolutional Networks. In *ICLR'20*, 2020. URL https://openreview.net/forum?id=S1e2agrFvS.

Bryan Perozzi, Vivek Kulkarni, Haochen Chen, and Steven Skiena. Don't walk, skip! online learning of multi-scale network embeddings. In *ASONAM '17*, pp. 258–265, 2017. URL https://doi.org/10.1145/3110025.3110086.

Oleg Platonov, Denis Kuznedelev, Michael Diskin, Artem Babenko, and Liudmila Prokhorenkova. A critical look at evaluation of gnns under heterophily: Are we really making progress? In *ICLR'23*, 2023. URL https://doi.org/10.48550/arXiv.2302.11640.

Emanuele Rossi, Bertrand Charpentier, Francesco Di Giovanni, Fabrizio Frasca, Stephan Günnemann, and Michael M Bronstein. Edge Directionality Improves Learning on Heterophilic Graphs. In *LoG '23*, 2023. URL https://doi.org/10.48550/arXiv.2305.10498.

Benedek Rozemberczki, Carl Allen, and Rik Sarkar. Multi-Scale attributed node embedding. *Journal of Complex Networks*, 9(2), 2021. URL https://doi.org/10.1093/comnet/cnab014.

Krzysztof Sadowski, Michał Szarmach, and Eddie Mattia. Dimensionality Reduction Meets Message Passing for Graph Node Embeddings. *ArXiv e-prints*, 2022. URL https://doi.org/10.48550/arXiv.2202.00408.

Vikram Saraph and Tijana Milenković. MAGNA: Maximizing Accuracy in Global Network Alignment. *Bioinformatics*, 30(20):2931–2940, 2014. URL https://doi.org/10.1093/bioinformatics/btu409.

Konstantinos Skitsas, Karol Orłowski, Judith Hermanns, Davide Mottin, and Panagiotis Karras. Comprehensive Evaluation of Algorithms for Unrestricted Graph Alignment. In *EDBT'23*, 2023. URL https://doi.org/10.48786/edbt.2023.21.

Jian Tang, Meng Qu, Mingzhe Wang, Ming Zhang, Jun Yan, and Qiaozhu Mei. Line: Large-Scale Information Network Embedding. In *WWW '15*, 2015. URL https://doi.org/10.1145/2736277.2741093.

Shantanu Thakoor, Corentin Tallec, Mohammad Gheshlaghi Azar, Mehdi Azabou, Eva L. Dyer, Remi Munos, Petar Veličković, and Michal Valko. Large-Scale Representation Learning on Graphs via Bootstrapping. In *ICLR'22*, 2022. URL https://doi.org/10.48550/arXiv.2102.06514.

Lloyd N. Trefethen and David Bau. *Numerical Linear Algebra*. Society for Industrial and Applied Mathematics, 1997. URL https://epubs.siam.org/doi/book/10.1137/1.9781611977165.

Petar Veličković, William Fedus, William L. Hamilton, Pietro Liò, Yoshua Bengio, and R Devon Hjelm. Deep Graph Infomax. In *ICLR'19*, 2019. URL https://openreview.net/forum?id=rklz9iAcKQ.

Petar Veličković, Guillem Cucurull, Arantxa Casanova, Adriana Romero, Pietro Liò, and Yoshua Bengio. Graph Attention Networks. In *ICLR '18*, 2018. URL https://openreview.net/forum?id=rJXMpikCZ.

Haonan Wang, Jieyu Zhang, Qi Zhu, Wei Huang, Kenji Kawaguchi, and Xiaokui Xiao. Single-Pass Contrastive Learning Can Work for Both Homophilic and Heterophilic Graph. *Transactions on Machine Learning Research*, 2023. URL https://openreview.net/forum?id=244KePn09i.

Felix Wu, Amauri Souza, Tianyi Zhang, Christopher Fifty, Tao Yu, and Kilian Weinberger. Simplifying Graph Convolutional Networks. In *ICML'19*, pp. 6861–6871, 2019. URL https://doi.org/10.48550/arXiv.1902.07153.

Zonghan Wu, Shirui Pan, Fengwen Chen, Guodong Long, Chengqi Zhang, and Philip S. Yu. A Comprehensive Survey on Graph Neural Networks. *IEEE Transactions on Neural Networks and Learning Systems*, 32(1): 4–24, 2021. URL https://doi.org/10.1109/TNNLS.2020.2978386.

Wenjian Yu, Yu Gu, Jian Li, Shenghua Liu, and Yaohang Li. Single-Pass PCA of Large High-Dimensional Data. In *IJCAI '17*, pp. 3350–3356, 2017. URL https://doi.org/10.24963/ijcai.2017/468.

Hengrui Zhang, Qitian Wu, Junchi Yan, David Wipf, and S Yu Philip. From Canonical Correlation Analysis to Self-supervised Graph Neural Networks. In *NeurIPS'21*, 2021. URL https://doi.org/10.48550/arXiv.2106.12484.

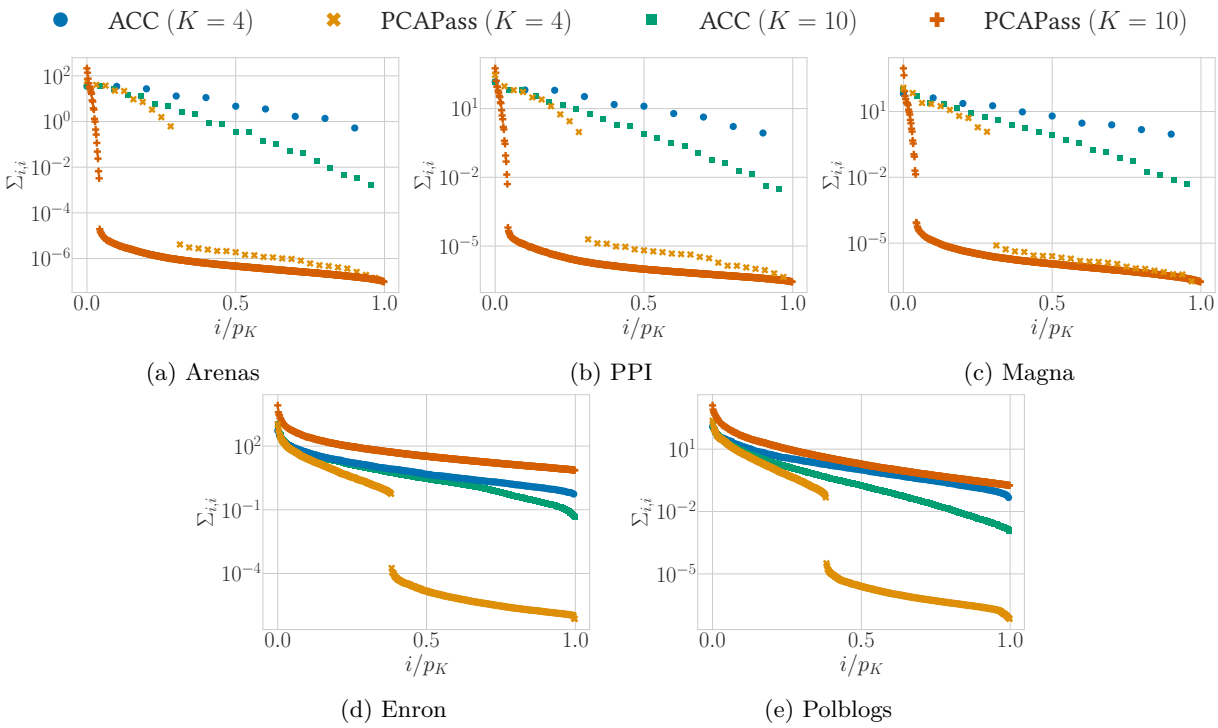

(a) Arenas (b) PPI (c) Magna

(d) Enron (e) Polblogs

Figure 7: The singular values spectrum for ACC and PCAPass on all graph alignment datasets. Spectrums using both $K = 4$ and $K = 10$ message-passing iterations are shown. The y-axes shows the singular values, and the x-axes their index in descending order, normalized using the number of embedding dimensions p_K.

A SVD of rank-deficient matrix

In Section 3.1, we stated the SVD of the matrix $\boldsymbol{Z} = \begin{bmatrix}\boldsymbol{X} & \boldsymbol{X}\end{bmatrix} \in \mathbb{R}^{n\times 2d}$, as $\boldsymbol{Z} = \boldsymbol{U_Z}\boldsymbol{\Sigma_Z}\boldsymbol{V_Z}^\intercal$, where

$$\boldsymbol{U_Z} = \begin{bmatrix}\boldsymbol{U} & \boldsymbol{\Upsilon_U}\end{bmatrix}, \qquad \boldsymbol{\Sigma_Z} = \begin{bmatrix}\sqrt{2}\boldsymbol{\Sigma} & \boldsymbol{0} \\ \boldsymbol{0} & \boldsymbol{0}\end{bmatrix}, \qquad \boldsymbol{V_Z}^\intercal = \frac{1}{\sqrt{2}}\begin{bmatrix}\boldsymbol{V}^\intercal & \boldsymbol{V}^\intercal \\ \boldsymbol{\Upsilon}_{\boldsymbol{V}_1}^\intercal & \boldsymbol{\Upsilon}_{\boldsymbol{V}_2}^\intercal\end{bmatrix}, \tag{12}$$

and the block matrices $\boldsymbol{\Upsilon_U} \in \mathbb{R}^{n\times d}$, $\boldsymbol{\Upsilon}_{\boldsymbol{V}_1} \in \mathbb{R}^{d\times d}$, and $\boldsymbol{\Upsilon}_{\boldsymbol{V}_2} \in \mathbb{R}^{d\times d}$ each have orthogonal columns and satisfy the conditions $\boldsymbol{\Upsilon}_{\boldsymbol{U}}^\intercal\boldsymbol{U} = \boldsymbol{0}$, $\boldsymbol{\Upsilon}_{\boldsymbol{U}}^\intercal\boldsymbol{\Upsilon_U} = \boldsymbol{I}$, $\boldsymbol{\Upsilon}_{\boldsymbol{V}_1}^\intercal\boldsymbol{V} = \boldsymbol{\Upsilon}_{\boldsymbol{V}_2}^\intercal\boldsymbol{V} = \boldsymbol{0}$, and $\boldsymbol{\Upsilon}_{\boldsymbol{V}_1}^\intercal\boldsymbol{\Upsilon}_{\boldsymbol{V}_1} = \boldsymbol{\Upsilon}_{\boldsymbol{V}_2}^\intercal\boldsymbol{\Upsilon}_{\boldsymbol{V}_2} = \boldsymbol{I}$.

Here, we verify the orthonormality of $\boldsymbol{U_Z}$ and $\boldsymbol{V_Z}$ via matrix multiplication:

$$\boldsymbol{U_Z}^\intercal\boldsymbol{U_Z} = \begin{bmatrix}\boldsymbol{U}^\intercal \\ \boldsymbol{\Upsilon}_{\boldsymbol{U}}^\intercal\end{bmatrix}\begin{bmatrix}\boldsymbol{U} & \boldsymbol{\Upsilon_U}\end{bmatrix} = \begin{bmatrix}\boldsymbol{U}^\intercal\boldsymbol{U} & \boldsymbol{U}^\intercal\boldsymbol{\Upsilon_U} \\ \boldsymbol{\Upsilon}_{\boldsymbol{U}}^\intercal\boldsymbol{U} & \boldsymbol{\Upsilon}_{\boldsymbol{U}}^\intercal\boldsymbol{\Upsilon_U}\end{bmatrix} = \begin{bmatrix}\boldsymbol{I} & \boldsymbol{0} \\ \boldsymbol{0} & \boldsymbol{I}\end{bmatrix}$$

$$\boldsymbol{V_Z}^\intercal\boldsymbol{V_Z} = \frac{1}{2}\begin{bmatrix}\boldsymbol{V}^\intercal & \boldsymbol{V}^\intercal \\ \boldsymbol{\Upsilon}_{\boldsymbol{V}_1}^\intercal & \boldsymbol{\Upsilon}_{\boldsymbol{V}_2}^\intercal\end{bmatrix}\begin{bmatrix}\boldsymbol{V} & \boldsymbol{\Upsilon}_{\boldsymbol{V}_1} \\ \boldsymbol{V} & \boldsymbol{\Upsilon}_{\boldsymbol{V}_2}\end{bmatrix} = \frac{1}{2}\begin{bmatrix}\boldsymbol{V}^\intercal\boldsymbol{V} + \boldsymbol{V}^\intercal\boldsymbol{V} & \boldsymbol{V}^\intercal\boldsymbol{\Upsilon}_{\boldsymbol{V}_1} + \boldsymbol{V}^\intercal\boldsymbol{\Upsilon}_{\boldsymbol{V}_2} \\ \boldsymbol{\Upsilon}_{\boldsymbol{V}_1}^\intercal\boldsymbol{V} + \boldsymbol{\Upsilon}_{\boldsymbol{V}_2}^\intercal\boldsymbol{V} & \boldsymbol{\Upsilon}_{\boldsymbol{V}_1}^\intercal\boldsymbol{\Upsilon}_{\boldsymbol{V}_1} + \boldsymbol{\Upsilon}_{\boldsymbol{V}_2}^\intercal\boldsymbol{\Upsilon}_{\boldsymbol{V}_2}\end{bmatrix} = \begin{bmatrix}\boldsymbol{I} & \boldsymbol{0} \\ \boldsymbol{0} & \boldsymbol{I}\end{bmatrix}.$$

B Singular values of ACC and PCAPass

Figure 7 presents the singular value spectra for the ACC and PCAPass embedding matrices across all graph alignment datasets. Both models use a maximum embedding dimension of $p_{\max} = 512$. However, this does not result in the same final embedding dimension, p_K, for each model. To facilitate comparison, we normalize the singular value index i (x-axis) by the embedding dimension.

For the undirected graphs (Arenas, PPI, and Magna), the singular value gap indicating rank deficiency is clearly visible for PCAPass, with both $K = 4$ and $K = 10$ message-passing iterations. On the directed graphs, this gap only appears for $K = 4$, consistent with the results in Figure 4c. In contrast, ACC shows no such singular value gaps, further confirming that it produces full-rank embeddings.

Table 2: Table 2a shows graph statistics for the graph alignment datasets. Specifically, it shows the number of nodes and edges, the number of weakly and strongly connected components, the global clustering coefficient, $C_{\mathcal{G}}$, and the average path length, $\langle l_{\text{path}} \rangle$. Table 2b shows basic information regarding the node classification datasets: the number of nodes, edges and node features, and the number of node classes.

(a) Graph alignment datasets and statistics.

Dataset	n	m	Dir.	# CC	# SCC	$C_{\mathcal{G}}$	$\langle l_{\text{path}} \rangle$
Arenas	1.1K	11K	✗	1	–	0.17	3.6
PPI	3.9K	76K	✗	35	–	0.09	3.1
PolBlogs	1.5K	19K	✓	268	688	0.25	3.4
Enron	7.9K	142K	✓	58	861	0.16	3.5
Magna	1K	17K	✗	1	–	0.62	5.5

(b) Node classification datasets.

Dataset	n	m	# Feat.	# Cls.
Chameleon	2.3K	36K	2325	5
Squirrel	5.2K	217K	2089	5
Roman Empire	23K	33K	300	18
Arxiv Year	169K	1.2M	128	5
Snap patents	2.9M	14M	269	5

C Additional experiments information and results

C.1 Datasets

Table 2a provides statistics for the graph alignment datasets. Arenas (Guimera et al., 2003) is an undirected email network, where each edge represents email communication between two students. Similar to Magna, PPI (Breitkreutz et al., 2007) is a protein-protein interaction graph, with nodes representing proteins and edges denoting interactions between them. Polblogs (Adamic & Glance, 2005) is a hyperlink graph of political blogs, while Enron (Klimt & Yang, 2004) is an email communication network, where each node corresponds to an email address. Specifically, we use a subgraph of the full Enron dataset for our experiments.

Table 2b summarizes the node classification datasets. These datasets were used in recent work by Rossi et al. (2023) on directed message-passing for supervised graph neural networks.

The Chameleon and Squirrel datasets are both hyperlink networks, where each node represents a Wikipedia article, and edges indicate hyperlinks between articles. Node features are binary variables indicating the presence of specific nouns, while labels reflect the average monthly traffic for each webpage. Originally proposed by Rozemberczki et al. (2021) for regression tasks, they were later adapted for node classification by Pei et al. (2020).

The Roman Empire dataset, introduced by Platonov et al. (2023), is a word co-occurrence network based on the Wikipedia page for the Roman Empire. Nodes correspond to words, and edges represent syntactic dependencies between them, resulting in a graph that closely resembles a chain structure. The node labels represent syntactic roles, while the features are word embeddings.

Arxiv Year and Snap Patents were introduced by Lim et al. (2021) to benchmark GNNs on large-scale graphs. The Arxiv Year dataset is derived from the OGB Arxiv citation network (Hu et al., 2020), where nodes represent papers and features are derived from their abstracts. Unlike OGB Arxiv, which uses subject areas for labels, Arxiv Year assigns labels based on the publication year.

Snap Patents is a patent citation network, where nodes represent patents and edges indicate citations. Originally studied by Leskovec et al. (2005) to investigate the evolution of citation networks over time, the dataset used by Lim et al. (2021) assigns labels based on the year each patent was granted. Node features are generated from patent metadata.

C.2 Additional graph alignment results

Figure 8 extends the results shown in Figure 6 from the main paper, now including the Arenas, PPI, and Polblogs datasets. The figure presents graph alignment accuracies and run times across varying relative tolerances θ for thresholding singular values.

The trends in accuracy and run time closely resemble those observed for Magna and Enron in Figure 6. Specifically, PCAPass can match ACC's accuracy within a certain range of θ values, but its accuracy sharply drops to zero outside this range. In contrast, ACC maintains stable accuracy, only declining for very

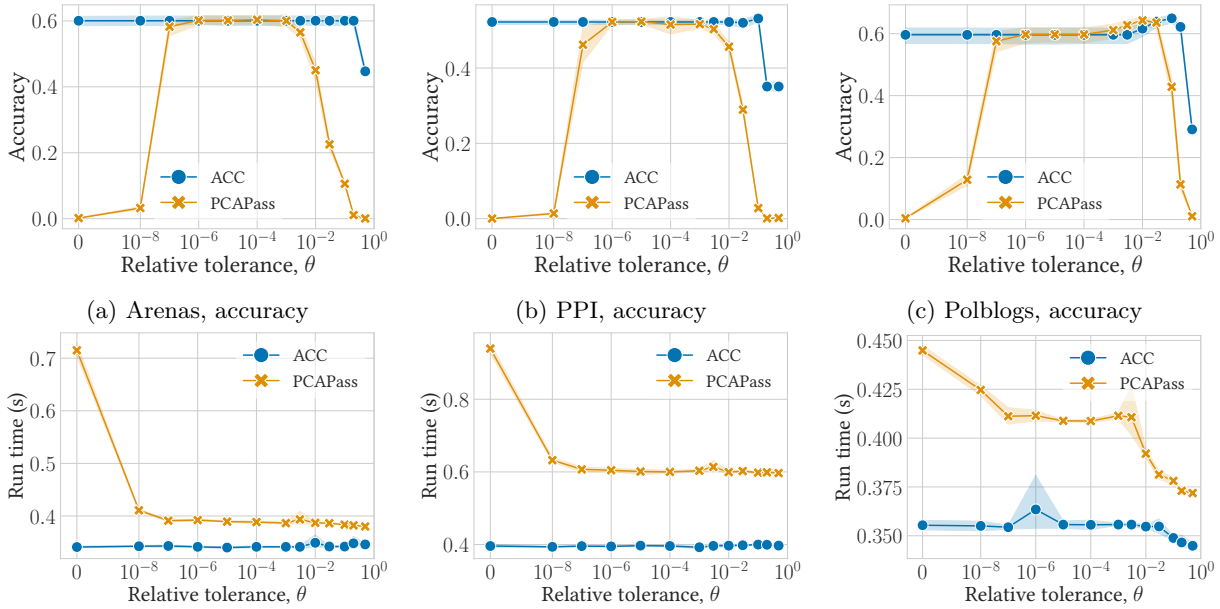

(a) Arenas, accuracy (b) PPI, accuracy (c) Polblogs, accuracy

(d) Arenas, run time (e) PPI, run time (f) Polblogs, run time

Figure 8: ACC and PCAPass for graph alignment with 15% noise edges, $K = 10$ for Arenas and PPI, and $K = 4$ for Polblogs. The x-axes show the relative tolerance θ applied to remove dimensions with small singular values. Figures 8a to 8c show accuracy on the y-axis, while 8d to 8f show run time. Markers and shaded areas indicate the average and standard deviation over 5 seeds.

high values of θ, which leads to excessive removal of embedding features. Additionally, ACC consistently outperforms PCAPass in terms of run time.

C.3 Node classification baselines

Below, we list the baselines used in our node classification experiment, including references to the respective model implementations and their licences. For models licensed under the MIT or Apache 2.0 licences, we also release our directed extensions as part of this paper's code repository. Additionally, we specify the default number of epochs used for training, as this directly influences the reported model run times. For other hyperparameter defaults, please refer to our code.

GAE (Kipf & Welling, 2017): `https://pytorch-geometric.readthedocs.io/en/latest/generated/torch_geometric.nn.models.GAE.html`, MIT Licence, 200 epochs.

DGI (Veličković et al., 2019): `https://github.com/PetarV-/DGI`, MIT licence, 100 epochs.

MVGRL (Hassani & Khasahmadi, 2020): `https://github.com/kavehhassani/mvgrl`, No licence, 3000 epochs.

BGRL (Thakoor et al., 2022): `https://github.com/nerdslab/bgrl`, Apache Licence 2.0, 10000 epochs.

CCA-SSG (Zhang et al., 2021): `https://github.com/hengruizhang98/CCA-SSG`, Apache Licence 2.0, 100 epochs.

GraphMAE (Hou et al., 2022): `https://github.com/THUDM/GraphMAE`, MIT licence, 1000 epochs.

GraphMAEv2 (Hou et al., 2023): `https://github.com/THUDM/GraphMAE2`, MIT licence, 1000 epochs.

GREET (Liu et al., 2023): `https://github.com/yixinliu233/GREET`, MIT licence, 400 epochs.

SPGCL (Wang et al., 2023): `https://github.com/haonan3/SPGCL`, No licence, 500 epochs.

Table 3: Node classification results using a logistic regression classifier. OOM abbreviates *out of memory*. All Snap Patents results were gathered using CPU only as the SSGNNs exceeded our GPU memory limit. The top 3 accuracies for each dataset are highlighted in bold.

Model	Chameleon		Squirrel		Roman Empire		Arxiv Year		Snap-Patents	
	Accuracy	Time	Accuracy	Time	Accuracy	Time	Accuracy	Time	Accuracy	Time
No model, **X**	52.3 ± 2.2	0ms	35.3 ± 1.4	0ms	69.8 ± 0.7	0ms	43.4 ± 0.2	0ms	50.7 ± 0.1	0ms
GAE[1]	54.8 ± 2.6	11s	38.2 ± 1.9	1m 4s	66.1 ± 1.8	16s	43.2 ± 0.3	7m 34s	49.3 ± 0.1	3h 15m
DGI[2]	54.0 ± 2.8	14s	40.4 ± 1.7	1m 40s	76.5 ± 0.7	4m 2s	$\mathbf{49.4 \pm 0.3}$	5h	Timeout	≥24h
MVGRL[3]	55.4 ± 3.0	26m 44s	40.0 ± 1.4	26m 32s	65.1 ± 0.9	39m 13s	OOM	≥128 GB	OOM	≥128 GB
BGRL[4]	55.9 ± 2.6	7m 49s	42.8 ± 1.5	31m 45s	$\mathbf{79.0 \pm 0.7}$	25m 24s	49.4 ± 0.3	4h 52m	Timeout	≥24h
BGRL-GS[4]	58.6 ± 2.1	8m 31s	41.6 ± 1.7	33m 21s	78.9 ± 0.7	21m 52s	47.8 ± 0.3	3h 8m	Timeout	≥24h
CCA-SSG[5]	59.5 ± 2.7	4s	41.6 ± 1.4	7s	70.0 ± 0.7	10s	$\mathbf{50.9 \pm 0.3}$	1m 11s	$\mathbf{55.3 \pm 0.1}$	1h 40m
GraphMAE[6]	$\mathbf{65.3 \pm 2.1}$	27s	$\mathbf{43.5 \pm 1.7}$	59s	55.7 ± 0.8	1m 8s	43.8 ± 0.3	8m 55s	44.1 ± 0.1	16h
GraphMAEv2[7]	$\mathbf{65.1 \pm 2.2}$	36s	40.4 ± 2.1	1m 14s	55.0 ± 0.9	1m 46s	44.1 ± 0.3	14m 53s	42.7 ± 0.1	23h
GraphMAEv2-GS[7]	$\mathbf{70.6 \pm 2.3}$	29s	$\mathbf{48.6 \pm 1.6}$	1m 6s	$\mathbf{80.2 \pm 0.7}$	1m 35s	46.9 ± 0.3	10m 46s	$\mathbf{54.7 \pm 0.0}$	18h
GREET[8]	53.9 ± 2.3	1m 25s	37.1 ± 1.5	6m 45s	77.5 ± 0.6	1h 56m	OOM	≥128 GB	OOM	≥128 GB
SPGCL[9]	58.2 ± 2.3	16s	42.5 ± 1.5	1m 23s	76.2 ± 0.7	55s	48.2 ± 0.3	52m 6s	OOM	≥128 GB
SGCN[10]	49.8 ± 2.7	374ms	35.3 ± 1.2	723ms	39.2 ± 0.7	393ms	43.2 ± 0.2	1s	42.3 ± 0.7	26s
PCAPass[11]	48.7 ± 2.1	2s	40.5 ± 1.3	22s	77.6 ± 0.7	852ms	49.3 ± 0.3	2s	54.5 ± 0.1	2m 20s
ACC	60.7 ± 2.5	1s	$\mathbf{44.1 \pm 1.4}$	1s	$\mathbf{79.3 \pm 0.6}$	432ms	$\mathbf{49.4 \pm 0.3}$	1s	$\mathbf{56.6 \pm 0.0}$	27s

[1] Kipf & Welling (2017) [2] Veličković et al. (2019) [3] Hassani & Khasahmadi (2020) [4] Thakoor et al. (2022) [5] Zhang et al. (2021) [6] Hou et al. (2022) [7] Hou et al. (2023) [8] Liu et al. (2023) [9] Wang et al. (2023) [10] Wu et al. (2019) [11] Sadowski et al. (2022)

SGCN (Wu et al., 2019): https://pytorch-geometric.readthedocs.io/en/latest/generated/torch_geometric.nn.conv.SGConv.html, MIT licence.

PCAPass (Sadowski et al., 2022): The original PCAPass implementation is available at https://github.com/krzysztof-daniell/PCAPass under the MIT License. However, we use our reimplementation for this paper, available alongside ACC in our online code repository.

C.4 Node classification results using logistic regression

Table 3 presents the node classification test accuracies for each embedding model and dataset using a *logistic regression* classifier. The experimental setup otherwise follows the description in Section 5.2. We observe that the accuracies obtained with logistic regression are generally lower than those achieved using the gradient boosting classifier in the main paper (Table 1). This is expected, as gradient boosting is a more expressive and less biased model capable of capturing highly non-linear class boundaries.

Overall, ACC embeddings perform competitively against the SSGNNs also using the logistic regression classifier, achieving the highest accuracy on Snap Patents, the second-highest on Arxiv Year and Roman Empire, and ranking third on Squirrel and fourth on Chameleon.

On the Chameleon and Squirrel datasets, we observe a notable drop in ACC's performance with logistic regression compared to gradient boosting: from 76.6% to 60.7% on Chameleon, and from 71.5% to 44.1% on Squirrel. A similar trend is seen for other linear embedding models like SGCN and PCAPass. This suggests that a non-linear classification model is necessary to fully exploit the information in these embeddings.

In contrast, the performance gap is smaller for several SSGNNs. For instance, GraphMAEv2-GS sees only a modest decline in accuracy from 74.1% to 70.6% on Chameleon. This indicates that the inherent non-linearity of GNNs can compensate for the simplicity of logistic regression. However, the extent to which this potential is realized depends on the specific GNN architecture and training, as many SSGNN models still achieve lower accuracies than ACC with logistic regression.

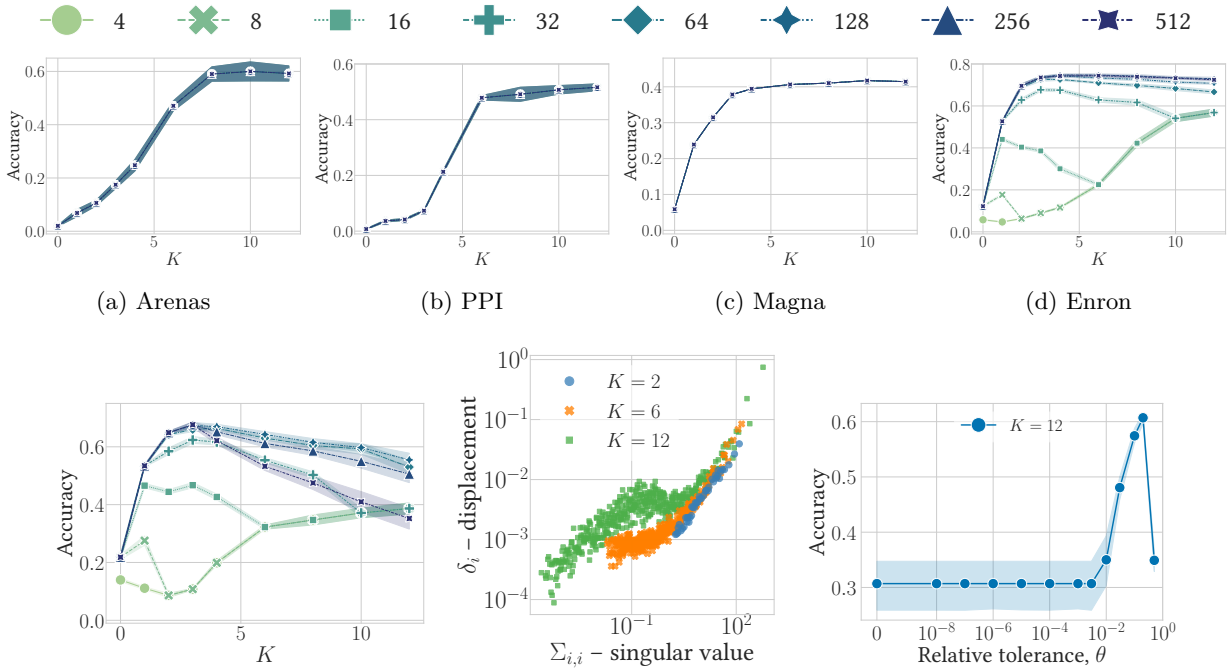

(a) Arenas (b) PPI (c) Magna (d) Enron

(e) Polblogs (f) Polblogs, ACC, $p_{\max} = 512$ (g) Polblogs, ACC, $p_{\max} = 512$

Figure 9: Figures 9a to 9e present the ACC graph alignment accuracy (y-axis) for varying numbers of message-passing iterations K (x-axis) and embedding dimensions $p_{\max}$ (indicated by hue and line style). Figures 9f and 9g provide deeper insights into the results for the Polblogs dataset. Similar to Figure 3c, Figure 9f plots the singular values of the embedding matrix (x-axis) against the average displacement along the corresponding principal axis, δ_i (y-axis). For $K = 6$ and $K = 12$, the correlation between singular value and displacement observed at $K = 2$ is disrupted, with some features exhibiting larger displacements than expected based on their singular values. These features cause the accuracy drop shown in Figure 9e. Finally, Figure 9g confirms that by removing the dimensions corresponding to these high-displacement, low-singular-value features, the alignment accuracy can be restored.

D Effect of the number of message-passing iterations and embedding dimensions

In this section, we investigate how the quality of ACC embeddings is influenced by the two primary hyperparameters: the number of message-passing iterations, K, and the maximum embedding dimensionality, $p_{\max}$. To assess their impact, we replicate the graph alignment and node classification experiments, measuring the accuracy of ACC embeddings across a grid of K and $p_{\max}$ values.

D.1 Graph Alignment

Figures 9a to 9e present the grid evaluation results for graph alignment, where the x-axes denote the number of message-passing iterations, K. The hue and line style differentiate the $p_{\max}$ values.

The first key observation is that accuracy increases steadily with K for each undirected graph, eventually plateauing. This illustrates ACC's ability to preserve information across multiple message-passing iterations.

Secondly, for the undirected graphs, the value of $p_{\max}$ appears to have no significant effect. This is because the initial number of features, $d = 2$, matches the minimum compression dimensionality, $c_{\min} = 2$, for these datasets. Therefore, regardless of the value of $p_{\max}$, the resulting ACC embeddings will have dimensionality $p_K = 2 \cdot (K + 1)$.

On the directed graphs, we observe different behaviour. Starting with Enron in Figure 9d, when $p_{\max}$ is sufficiently high, the accuracy follows a similar pattern to the undirected graphs, increasing steadily before levelling off. However, for $p_{\max} \in 8, 16, 32$, a different trend emerges: the accuracy initially increases, but then decreases, eventually aligning with the curve for $p_{\max} = 4$.

This seemingly unusual behaviour stems from the formula used to determine the number of compression dimensions, $c = \max\left(\lfloor p_{\max}/(K+1) \rfloor, c_{\min}\right)$, which in turn defines the final embedding dimensionality, $p_K = c \cdot (K+1)$. As K increases, this formula can lead to a decrease in the final embedding dimensionality, p. Consequently, more information must be compressed into fewer dimensions, resulting in a loss of information and a corresponding drop in accuracy. However, once $K+1$ becomes a factor of $p_{\max}$, the value of p_K increases again, restoring some of the lost accuracy.

For example, with $p_{\max} = 8$, we obtain $p_0 = 6$ and $p_1 = 8$ for $K = 0$ and $K = 1$, but then $p_2 = 6$ for $K = 2$, before increasing again to $p_3 = 8$. Beyond $K \geq 4$, the formula sets $c = c_{\min} = 2$, which is why the curve for $p_{\max} = 8$ converges with the curve for $p_{\max} = 4$. A similar explanation applies to the curves for $p_{\max} \in 16, 32$, as shown in Figure 9d.

In Figure 9e, we observe the same effect for $p_{\max} \in \{8, 16, 32\}$ on Polblogs as we did for Enron. However, we also notice a distinctly different behaviour: as K increases, the accuracy begins to drop for $p_{\max} \geq 64$.

This decline in accuracy is neither due to information loss from compression nor rank deficiency. As seen in Figure 7e, the singular value spectrum for ACC on Polblogs with $K = 10$ does not exhibit any singular value gaps. Instead, the drop in accuracy occurs because increasing K generates embedding features that are disproportionately noisy.

We demonstrate this effect in Figure 9f. Similar to Figures 3c and 3d in the main paper, Figure 9f plots the singular values of the embedding matrix against the average displacement along the corresponding principal axis due to noise from graph alignment. As a reminded from the main paper, let $\boldsymbol{Z}^{(1)}$ represent the embedding matrix for graph $\mathcal{G}_1$, and $\boldsymbol{Z}^{(2)}$ the embedding matrix for the noisy graph $\mathcal{G}_2$. Using the singular value decomposition $\boldsymbol{U}, \boldsymbol{\Sigma}, \boldsymbol{V}^\intercal = \boldsymbol{Z}^{(1)}$, where $\boldsymbol{V}$ contains the principal axes for $\boldsymbol{Z}^{(1)}$, the x-axis shows the singular values $\Sigma_{i,i}$, and the y-axis shows the displacement $\delta_i = \frac{1}{n}\|(\boldsymbol{Z}^{(1)} - \boldsymbol{Z}^{(2)})\boldsymbol{V}_{:,i}\|_2$ along the ith principal axis.

For $K = 2$, we observe that the displacement δ_i is proportional to the singular values $\Sigma_{i,i}$, consistent with our observations across the other four graph alignment datasets. However, for $K = 6$ and $K = 10$, this linear correlation breaks down, and features with disproportionately large displacements emerge. This is seen as the curvature of the point clouds in Figure 9f.

We further verify that these high-displacement features cause the accuracy drop by applying singular value thresholding. The results for $K = 12$ and $p_{\max} = 512$ are shown in Figure 9g. As can be seen, the alignment accuracy improves dramatically, from 30% to 60%, once the dimensions with small singular values and high displacements are removed.

We do not yet fully understand why the high-displacement dimensions appear in the Polblogs embeddings. Looking at the graph statistics in Table 2a, two potential causes stand out: the large number of weakly connected components and the high global clustering coefficient for Polblogs. However, we can rule out the former, as we observe the same behaviour when running the graph alignment experiment on the largest connected component of Polblogs. This leaves the high global clustering coefficient as the most likely cause. Further research is needed to verify this hypothesis and to explore the underlying mechanisms that might lead to the emergence of these high-displacement dimensions.

D.2 Node classification

Figure 10 illustrates the effect of K and $p_{\max}$ on ACC node classification accuracies, measured using a logistic regression classifier. Regarding $p_{\max}$, we observe a consistent increase in accuracy across all values of K. This is expected, as higher embedding dimensionality allows the embeddings to capture more information, facilitating better classification performance.

The effect of increasing the number of message-passing iterations K depends on the embedding dimensionality $p_{\max}$. When $p_{\max}$ is sufficiently large, classification accuracy rises and eventually plateaus for all four datasets.

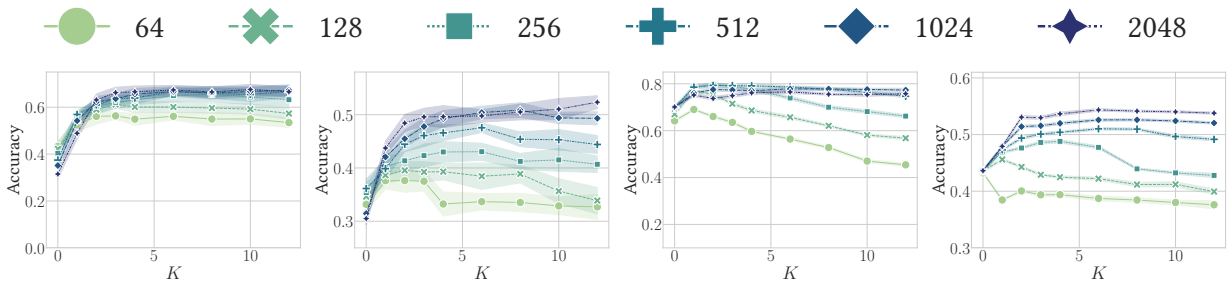

(a) Chameleon (b) Squirrel (c) Roman Empire (d) Arxiv Year

Figure 10: These figures the ACC node classification accuracy (y-axis) for various number of message-passing iterations K (x-axis), and embedding dimensions $p_{\max}$ (hue and style).

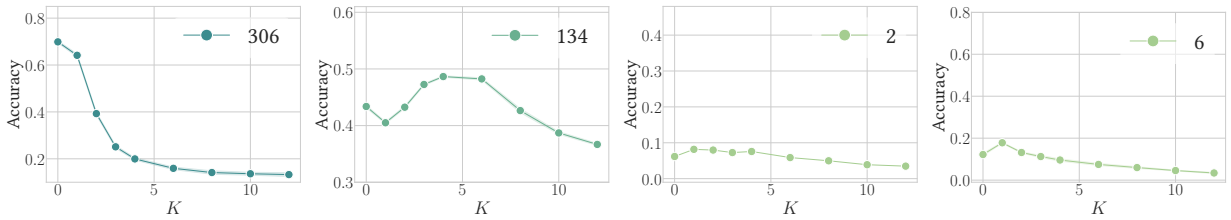

(a) Roman Empire (b) Arxiv Year (c) Magna (d) Enron

Figure 11: These figures show the SGCN (Wu et al., 2019) node classification accuracy (Figures 11a and 11b) and graph alignment accuracy (Figures 11c and 11d) on the y-axis, plotted against the number of message-passing iterations K (x-axis). The legends indicate the number of SGCN embedding dimensions, which are always equal to the number of input features d.

However, when $p_{\max}$ is too small, accuracy can decline as K increases. This effect is particularly notable for the Roman Empire dataset, as seen in Figure 10c.

The drop in accuracy is due to the increased need for compression as K grows, meaning that less information from each scale of the graph is retained. Specifically, when $K = 0$, the initial d features are compressed into $p_{\max}$ embedding dimensions, but when $K = 12$, these features are compressed into only $\lfloor p_{\max}/13 \rfloor$ dimensions. The loss of information due to this increased compression results in an accuracy decline for datasets where local features (i.e., small K) are especially important for classification. The Roman Empire dataset exemplifies this behaviour, where the information contained in $\boldsymbol{X}$, $\boldsymbol{A}_{\mathrm{F}}\boldsymbol{X}$, and $\boldsymbol{A}_{\mathrm{B}}\boldsymbol{X}$ is critical for achieving high accuracy.

D.3 Over-smoothing in SGCN

To highlight the advantage of the concatenation update used by ACC, we provide results using SGCN (Wu et al., 2019) in Figure 11. SGCN employs summation rather than concatenation to update its embeddings. This results in a loss of information with each message-passing iteration, leading to over-smoothing (Li et al., 2018; Chen et al., 2020).

This issue is particularly noticeable on the Roman Empire dataset, where the accuracy of SGCN drops from 70% to 10% as K increases. In contrast, ACC's accuracy remains stable as long as a sufficiently high embedding dimension is used, as shown in Figure 10c.

Additionally, SGCN embeddings maintain a fixed dimension for all message-passing iterations, $p_K = d$. This limitation hampers graph alignment accuracy, as it prevents the integration of information from different scales to form more distinct embeddings. Consequently, the alignment accuracy for SGCN is lower, as evidenced in Figures 11c and 11d.

E Analysis of node classification accuracy on the Squirrel dataset

In our node classification benchmark results using the gradient boosting classifier, as shown in Table 1, ACC achieves an accuracy of 72% on the Squirrel dataset, whereas PCAPass achieves only 52%. In this section, we explore the source of this discrepancy by analysing the Squirrel dataset and comparing the features generated by message aggregation and embedding aggregation.

To identify the key features contributing to high classification accuracy on Squirrel, we perform a single message-passing iteration to obtain three feature matrices: $\boldsymbol{X} \in \mathbb{R}^{n\times d}$, $\boldsymbol{A}_{\mathtt{F}}\boldsymbol{X} \in \mathbb{R}^{n\times d}$, and $\boldsymbol{A}_{\mathtt{B}}\boldsymbol{X} \in \mathbb{R}^{n\times d}$. We refer to these as *feature groups*.

By training a gradient boosting classifier on each feature group with an 80-20 training-test split, we find the following test accuracies: 51% for $\boldsymbol{X}$, 33% for $\boldsymbol{A}_{\mathtt{F}}\boldsymbol{X}$, and 84% for $\boldsymbol{A}_{\mathtt{B}}\boldsymbol{X}$. These results indicate that the features in $\boldsymbol{A}_{\mathtt{B}}\boldsymbol{X}$ are particularly crucial for achieving high classification accuracy on the Squirrel dataset.

Next, we investigate how well each feature group is preserved in the PCAPass and ACC embeddings. Ignoring the column centring step of PCA, we can express the PCAPass embeddings after one message-passing iteration as

$$\boldsymbol{Z} = \boldsymbol{H}^{(1)} = [\boldsymbol{X}, \boldsymbol{A}_{\mathtt{F}}\boldsymbol{X}, \boldsymbol{A}_{\mathtt{B}}\boldsymbol{X}]\boldsymbol{W} = \boldsymbol{X}\boldsymbol{W}_X + \boldsymbol{A}_{\mathtt{F}}\boldsymbol{X}\boldsymbol{W}_{\mathtt{F}} + \boldsymbol{A}_{\mathtt{B}}\boldsymbol{X}\boldsymbol{W}_{\mathtt{B}}, \qquad \boldsymbol{W} = \begin{bmatrix} \boldsymbol{W}_X \\ \boldsymbol{W}_{\mathtt{F}} \\ \boldsymbol{W}_{\mathtt{B}} \end{bmatrix}, \tag{13}$$

where $\boldsymbol{W} \in \mathbb{R}^{3d\times p}$ is the projection matrix learned via PCA. We divide this matrix vertically into three submatrices: $\boldsymbol{W}_X \in \mathbb{R}^{d\times p}$, $\boldsymbol{W}_{\mathtt{F}} \in \mathbb{R}^{d\times p}$, and $\boldsymbol{W}_{\mathtt{B}} \in \mathbb{R}^{d\times p}$. These matrices compress $\boldsymbol{X}$, $\boldsymbol{A}_{\mathtt{F}}\boldsymbol{X}$, and $\boldsymbol{A}_{\mathtt{B}}\boldsymbol{X}$ respectively. By analysing these matrices, we can assess how much information from each feature group is preserved.

Specifically, for each of the $p = 512$ features, we compute the proportion of each feature group that contributes to the embedding. Since each column in $\boldsymbol{W}$ has unit norm, these proportions can be calculated as follows:

$$\mathbf{w}_X = \sum_{i=1}^{d} (\boldsymbol{W}_X)_{i,:}^2, \qquad \mathbf{w}_{\mathtt{F}} = \sum_{i=1}^{d} (\boldsymbol{W}_{\mathtt{F}})_{i,:}^2, \qquad \mathbf{w}_{\mathtt{B}} = \sum_{i=1}^{d} (\boldsymbol{W}_{\mathtt{B}})_{i,:}^2, \tag{14}$$

where $\mathbf{w}_X$, $\mathbf{w}_{\mathtt{F}}$, and $\mathbf{w}_{\mathtt{B}}$ denote the proportions of each feature group represented in the embeddings. Note that $\mathbf{w}_X + \mathbf{w}_{\mathtt{F}} + \mathbf{w}_{\mathtt{B}} = \mathbf{1}_p$, where $\mathbf{1}_p$ is a length-p vector of ones.

We can perform a similar analysis for ACC. In this case, the embeddings are given by $\boldsymbol{Z} = [\boldsymbol{M}^{(0)}, \boldsymbol{M}^{(1)}]$, where $\boldsymbol{M}^{(0)} = \boldsymbol{X}\boldsymbol{V}_X$ and

$$\boldsymbol{M}^{(1)} = [\boldsymbol{A}_{\mathtt{F}}\boldsymbol{M}^{(0)}, \boldsymbol{A}_{\mathtt{B}}\boldsymbol{M}^{(0)}]\boldsymbol{V} = \boldsymbol{A}_{\mathtt{F}}\boldsymbol{X}\boldsymbol{V}_X\boldsymbol{V}_{\mathtt{F}} + \boldsymbol{A}_{\mathtt{B}}\boldsymbol{X}\boldsymbol{V}_X\boldsymbol{V}_{\mathtt{B}}, \qquad \boldsymbol{V} = \begin{bmatrix} \boldsymbol{V}_{\mathtt{F}} \\ \boldsymbol{V}_{\mathtt{B}} \end{bmatrix}. \tag{15}$$

Here, the matrices $\boldsymbol{V}_X \in \mathbb{R}^{d\times c}$, $\boldsymbol{V}_X\boldsymbol{V}_{\mathtt{F}} \in \mathbb{R}^{d\times c}$, and $\boldsymbol{V}_X\boldsymbol{V}_{\mathtt{B}} \in \mathbb{R}^{d\times c}$ are used to compress the three feature groups.

An important difference from PCAPass is that $\boldsymbol{V}_X$ is computed separately via PCA from $\boldsymbol{V}_{\mathtt{F}}$ and $\boldsymbol{V}_{\mathtt{B}}$, meaning that $\boldsymbol{V}_X$ forms an orthogonal basis by itself, i.e., $\boldsymbol{V}_X^{\intercal}\boldsymbol{V}_X = \boldsymbol{I}_c$. Consequently, the column norms of $\boldsymbol{V}_X\boldsymbol{V}_{\mathtt{F}}$ are equal to the column norms in $\boldsymbol{V}_{\mathtt{F}}$, and similarly for $\boldsymbol{V}_X\boldsymbol{V}_{\mathtt{B}}$ and $\boldsymbol{V}_{\mathtt{B}}$. This can be demonstrated by considering the norm of the ith column in $\boldsymbol{V}_X\boldsymbol{V}_{\mathtt{F}}$:

$$\|\boldsymbol{V}_X\boldsymbol{V}_{\mathtt{F}i,:}\|_2^2 = \boldsymbol{V}_{\mathtt{F}i,:}^{\intercal}\boldsymbol{V}_X^{\intercal}\boldsymbol{V}_X\boldsymbol{V}_{\mathtt{F}i,:} = \boldsymbol{V}_{\mathtt{F}i,:}^{\intercal}\boldsymbol{I}_c\boldsymbol{V}_{\mathtt{F}i,:} = \|\boldsymbol{V}_{\mathtt{F}i,:}\|_2^2. \tag{16}$$

Therefore, the ACC proportion vectors are

$$\mathbf{v}_X = \sum_{i=1}^{d} \left(\boldsymbol{V}_{Xi,:}\right)^2 = \mathbf{1}_c, \qquad \mathbf{v}_{\mathtt{F}} = \sum_{i=1}^{c} \left(\boldsymbol{V}_{\mathtt{F}i,:}\right)^2, \qquad \mathbf{v}_{\mathtt{B}} = \sum_{i=1}^{c} \left(\boldsymbol{V}_{\mathtt{B}i,:}\right)^2, \tag{17}$$

where $\mathbf{v}_{\mathtt{F}} + \mathbf{v}_{\mathtt{B}} = \mathbf{1}_c$.

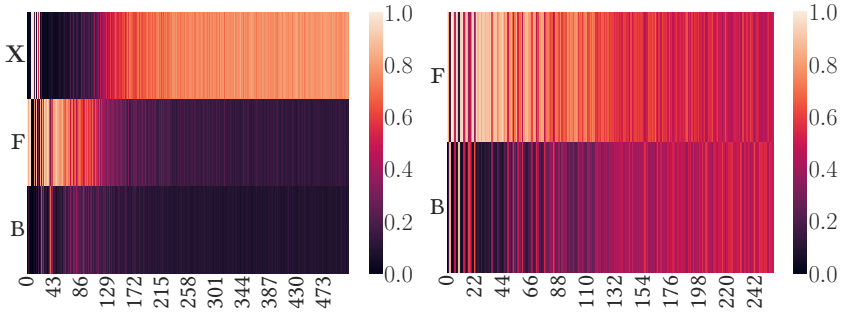

(a) PCAPass (b) ACC

Figure 12: Visualization of the projection matrices used in the first message-passing iteration for PCAPass and ACC. Each column represents an embedding dimension, while each row corresponds to one of three feature groups: the input features $\boldsymbol{X}$, the forward aggregation features $\boldsymbol{A}_{\mathtt{F}}\boldsymbol{X}$, and the backward aggregation features $\boldsymbol{A}_{\mathtt{B}}\boldsymbol{X}$. The colour indicates the proportion of each feature group represented in each embedding dimension. These proportions are calculated using Equations 14 and 17.

Model	$p_X^{(\text{eff})}$	$p_{\mathtt{F}}^{(\text{eff})}$	$p_{\mathtt{B}}^{(\text{eff})}$
PCAPass	309	140	63
ACC	256	160	96

Table 4: The effective number of embedding dimensions used per feature group after one message-passing iteration using ACC and PCAPass. The effective dimensions are calculated using Equations 18 and 19.

In Figure 12, we visualize the proportion vectors as heat maps. The heat maps on the left show the PCAPass vectors, $\mathbf{w}_X$, $\mathbf{w}_{\mathtt{F}}$, and $\mathbf{w}_{\mathtt{B}}$, while the heat maps on the right display the ACC vectors, $\mathbf{v}_{\mathtt{F}}$ and $\mathbf{v}_{\mathtt{B}}$. The colours in the heat maps represent the proportion of information derived from each feature group. The bright colours in the first two rows for PCAPass indicate that most of the information is captured from the features in $\boldsymbol{X}$ and $\boldsymbol{A}_{\mathtt{F}}\boldsymbol{X}$. In contrast, ACC captures more information from $\boldsymbol{A}_{\mathtt{B}}\boldsymbol{X}$, as evidenced by the more uniform colour distribution in its heat map.

We can further quantify this difference by computing the effective number of features extracted from each feature group. We denote this as $p_*^{(\text{eff})}$, where the star is either X, $\mathtt{F}$, or $\mathtt{B}$ for each respective feature group. These quantities are computed as the sum of each proportion vector:

$$p_X^{(\text{eff})} = \sum_{k=1}^{p} w_{X\,k}, \qquad p_{\mathtt{F}}^{(\text{eff})} = \sum_{k=1}^{p} w_{\mathtt{F}k}, \qquad p_{\mathtt{B}}^{(\text{eff})} = \sum_{k=1}^{p} w_{\mathtt{B}k}, \tag{18}$$

for PCAPass, and

$$p_X^{(\text{eff})} = \sum_{k=1}^{c} v_X = 256, \qquad p_{\mathtt{F}}^{(\text{eff})} = \sum_{k=1}^{c} v_{\mathtt{F}k}, \qquad p_{\mathtt{B}}^{(\text{eff})} = \sum_{k=1}^{c} v_{\mathtt{B}k}, \tag{19}$$

for ACC. Note that $p_X^{(\text{eff})} = c = 256$ since ACC always includes c features per message-passing iteration.

The effective number of embedding dimensions is shown in Table 4. Compared to PCAPass, ACC effectively uses 53 fewer features from $\boldsymbol{X}$ and 33 more features from $\boldsymbol{A}_{\mathtt{B}}\boldsymbol{X}$, which represents more than a 50% increase compared to 63 for PCAPass. The inclusion of these class-informative features explains the higher accuracy achieved by message aggregation compared to embedding aggregation on the Squirrel dataset.